

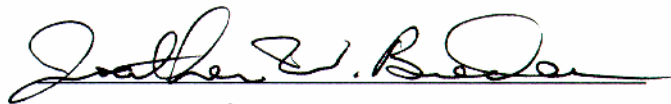
A PHYSICS BASED MULTI-RESOLUTION TECHNIQUE
FOR EXTRACTION OF FINITE DURATION
TIME RESPONSES IN RADAR IMAGES

The members of the Committee approve the master's
thesis of Nancy E. Lanett

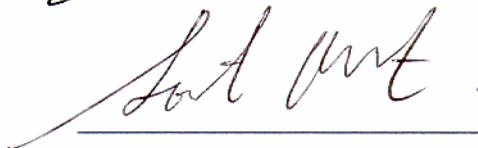
Saibun Tjuatja
Supervising Professor



Jonathan W. Bredow



Soontorn Oraintara



to my son

A PHYSICS BASED MULTI-RESOLUTION TECHNIQUE
FOR EXTRACTION OF FINITE DURATION
TIME RESPONSES IN RADAR IMAGES

by

NANCY E. LANETT

Presented to the Faculty of the Graduate School of
The University of Texas at Arlington in Partial Fulfillment
of the Requirements
for the Degree of

MASTER OF SCIENCE IN ELECTRICAL ENGINEERING

THE UNIVERSITY OF TEXAS AT ARLINGTON

May 2006

ACKNOWLEDGEMENTS

I would like to express my sincere appreciation to Dr. Saibun Tjuatja for his motivation and support for this thesis. I would also like to thank Dr. Jonathan Bredow for providing insight to the measurement techniques used to acquire the data and Dr. Soontorn Orintara for providing necessary support. Thanks also go to Suman Kumar Gunnala who performed the measurements and provided the data.

Special thanks to my co-workers at Raytheon Advanced Products Center for providing the encouragement and support for me to complete my degree. Finally, I would like to thank my family and friends for their love and support and for encouraging my seemingly endless pursuit of higher education.

December 9, 2005

ABSTRACT

A PHYSICS BASED MULTI-RESOLUTION TECHNIQUE FOR EXTRACTION OF FINITE DURATION TIME RESPONSES IN RADAR IMAGES

Publication No. _____

Nancy E. Lanett, M.S.

The University of Texas at Arlington, 2006

Supervising Professor: Saibun Tjuatja

This paper presents a wavelet multi-resolution technique for examination of scattering phenomena in radar images. Through multi-resolution frequency domain analysis, range gating is implemented for extraction of wave medium interaction phenomena. To analyze the data, a sliding range gate is implemented by applying a phase shift to the spectral domain far field data prior to wavelet analysis. A method for efficient removal of window effects, which occur due to the finite nature of the data, is demonstrated through reconstruction of the decomposed waveform following removal of the lowest resolution. A correlation of the physical meaning of the multi-resolution

data to scattering interactions is demonstrated for several test cases consisting of metallic targets. Results and representative images, reconstructed from the experimental scattering data, demonstrate that the proposed approach provides a means to examine scattering phenomena at different instances in time.

TABLE OF CONTENTS

ACKNOWLEDGEMENTS.....	iv
ABSTRACT	v
LIST OF FIGURES	ix
LIST OF TABLES.....	xii
CHAPTER	
1 INTRODUCTION	1
2 BACKGROUND	4
2.1 ISAR Imaging.....	4
2.2 Window Effects	7
2.3 Range Gating	9
2.4 Wavelets.....	10
2.5 Multi-Resolution Frequency Domain Analysis	14
2.5.1 Implementation	14
2.5.2 Physical Meaning.....	17
3 METHODOLOGY	21
3.1 Data Collection	21
3.2 Data Processing.....	24
3.2.1 Removal of Windowing Effects	27
3.2.2 Sliding Gate Implementation.....	28

3.2.3 ISAR Images.....	30
4 EXPERIMENTAL RESULTS AND DISCUSSION	32
4.1 Removal of Window Effects.....	32
4.2 Physical Meaning of Resolutions	34
4.2.1 Scattering Phenomena from a Metal Sphere	35
4.2.2 Scattering Phenomena from a Triangular Target.....	38
4.2.3 Scattering Phenomena from Multiple Targets.....	42
4.3 Implementation of Sliding Gate.....	48
4.3.1 Gated Scattering Response Metal Sphere.....	48
4.3.2 Gated Scattering Response Metal Triangle	51
4.3.3 Gated Scattering Response Multiple Targets	55
5 CONCLUSIONS	61
APPENDIX	
A MATHEMATICA MULTI-RESOLUTION PROGRAM	65
B MATHEMATICA CALIBRATION PROGRAM.....	69
C MATHEMATICA POLAR FORMAT PROGRAM	72
D MATHEMATICA ISAR PROGRAM	75
E MATHEMATICA PROGRAM SPHERE THEORETICAL SCATTERING.....	77
REFERENCES	79
BIOGRAPHICAL INFORMATION.....	81

LIST OF FIGURES

Figure	Page
2.1 Data Format (a) Frequency Domain, (b) K-Space Domain, and (c) Spatial Domain	6
2.2 Window Effects (a) K-Space and (b) Spatial Domain.....	8
2.3 Range Gating for Clutter Rejection	9
2.4 Block Diagram of a 5-Level Orthogonal Wavelet Decomposition	13
2.5 Block Diagram of a 5-Level Orthogonal Wavelet Reconstruction	13
2.6 Segmentation of Time Domain.....	15
2.7 Multi-Resolution Frequency Domain Analysis.....	17
2.8 Time Domain Response at a Single Look Angle (a) Approximation 3, (b) Details 3-5 and (c) Details 6-7 using Daub4 with 8 Decompositions	18
2.9 Time Domain Response, a_1 , prior to phase shift	19
2.10 Time domain response, a_1 , for $t_0 = 1.0 \cdot ns$	20
3.1 RCS Measurement Test Units (a) Sphere, (b) Triangular and (c) Sphere & Triangular Targets	22
3.2 Broadband Dual Polarization Conical Horns	23
3.3 RCS Measurement Setup.....	24
3.4 Multi-Resolution ISAR Imaging Flow Chart	25
3.5 Sliding Gate Spatial Domain Response with a_1 (bold) for Initial Shift (a) $t_0 = 0.5ns$ and (b) $t_0 = 1.5ns$	29

3.6	Sliding Gate Spatial Domain Response with a_1 (bold) for Conjugate Shift (a) $t_0 = -0.5ns$ and (b) $t_0 = -1.5ns$	30
3.7	Multi-Resolution ISAR Images Metal Sphere (a) Approximation 1 and (b-f) Details 1-5.....	31
4.1	Multi-Resolution ISAR Images Prior to Removal of Window Effects	33
4.2	ISAR Images (a) Initial, (b) Approximation 1 and (b) Details 1-9	34
4.3	ISAR Image 4" Metal Sphere	36
4.4	Cross Range Image ($downrange = 0$) 4" Metal Sphere.....	36
4.5	Time Domain Representation Approximation 1 and Details 1-5	37
4.6	Multi-Resolution ISAR Images Metal Sphere (a) Approximation 1 and (b-f) Details 1-5.....	38
4.7	Scattering Geometry for Metal Triangular Target.....	39
4.8	ISAR Image Metal Triangular Target.....	40
4.9	Cross Range Image ($downrange = 0$) of Metal Triangular Target.....	40
4.10	Multi-Resolution ISAR Images Triangular Target (a) Approximation 1 and (b-f) Details 1-5.....	41
4.11	ISAR Image Sphere and Triangle Targets, $dz = 7"$	43
4.12	Cross Range Image ($downrange = 0$) of Sphere and Triangle, $dz = 7"$	43
4.13	Multi-Resolution ISAR Images Metal Sphere & Triangle $dz = 7"$ (a) Approximation 1 and (b-f) Details 1-5	44
4.14	ISAR Image Sphere and Triangle Targets, $dz = 11"$	46
4.15	Cross Range Image ($downrange = 0$) of Sphere and Triangle, $dz = 11"$	46
4.16	Multi-Resolution ISAR Images Metal Sphere & Triangle $dz = 11"$ (a) Approximation 1 and (b-f) Details 1-5	47

4.17	Multi-Resolution ISAR Images Metal Sphere $t_0 = 0.5ns$ (a) Approximation 1 and (b-f) Details 1-5	49
4.18	Time Domain Representation of Gating.....	50
4.19	Time Domain Representation of Sliding Gate.....	51
4.20	ISAR Images Metal Sphere d_1 with progressive shifts $t_0 = 0$ to $9\Delta t$, $\Delta t = 0.125ns$	51
4.21	Multi-Resolution ISAR Images Triangular Target ($t_0 = 0.5ns$) (a) Approximation 1 and (b-f) Details 1-5	52
4.22	Time Domain Representation of Sliding Gate.....	54
4.23	ISAR Images Metal Triangular Target d_1 with progressive shifts $t_0 = 0$ to $19\Delta t$, $\Delta t = 0.125ns$	54
4.24	Multi-Resolution ISAR Images Metal Sphere & Triangle $dz = 7''$ ($t_0 = 0.5ns$) (a) Approximation 1 and (b-f) Details 1-5	55
4.25	Multi-Resolution ISAR Images Metal Sphere & Triangle $dz = 7''$ ($t_0 = 1.25ns$) (a) Approximation 1 and (b-f) Details 1-5	56
4.26	Multi-Resolution ISAR Images Metal Sphere & Triangle $dz = 11''$ ($t_0 = 0.5 \cdot ns$) (a) Approximation 1 and (b-f) Details 1-5.....	57
4.27	Multi-Resolution ISAR Images Metal Sphere & Triangle $dz = 11''$ ($t_0 = 1.25ns$) (a) Approximation 1 and (b-f) Details 1-5	58
4.28	Time Domain Representation of Sliding Gate.....	59
4.29	ISAR Images Sphere and Triangle ($dz = 11''$) d_1 with progressive shifts $t_0 = 0$ to $19\Delta t$, $\Delta t = 0.125ns$	60

LIST OF TABLES

Table	Page
3.1 Experimental Test Cases.....	21
3.2 Test Parameters.....	23
3.3 Time Gate Widths for Daub2, 9 Decompositions, $\Delta t=0.125$ ns, 1024 points	27
3.4 Spatial Gate Widths for Daub2, 9 Decompositions, $\Delta s=1.5$ ", 1024 points	27

CHAPTER 1

INTRODUCTION

Microwave imaging techniques are used in many applications but all encounter the same challenge of extracting information from a signal that contains noise, clutter effects and interactions from multiple scattering sources. Imaging techniques are used for diagnostic purposes or real time applications. Regardless of the application, microwave imaging provides a means to either characterize or identify an object irradiated by electromagnetic energy. Data collection is performed in different manners but the fundamentals are the same. A relationship exists between the scattered electric fields, which can be determined through measurements, and an object's reflectivity [1]. The phase of the scattered signal contains information that relates spatially to the currents induced on the irradiated object. Images are produced by taking advantage of the phase differences that result from an object's frequency dependent reflectivity as well as relative motion between the target and the antenna.

The motivation of this work is to further investigate the use of multi-resolution wavelet analysis techniques to examine scattering phenomena in radar images. Multi-resolution analysis can be used to reduce clutter through selection of resolutions corresponding to scattering phenomena which occur at earlier or later arrival times [2]. In order to generate an image, range gating of the data is performed to remove clutter

and isolate scattering sources to resolve the target. Utilization of wavelet analysis provides an efficient means to implement gating techniques.

For full analysis of the data, it is necessary to selectively position the range gate. Phase shifts applied in the frequency domain, prior to wavelet analysis, allow for selection of different instances in time for separation of scattering centers and for visualization of the evolution of the scattered fields in time. The ability to extract wave medium interactions through selective application of range gates increases the capability to identify or characterize targets. Application of the wavelet transform to phase shifted frequency domain signal, is an efficient means to implement a sliding range gate. Evaluation of the scattering properties of an object is possible through correlation of the physical meaning of the multi-resolution data to the observed responses in the image.

Standard Inverse Synthetic Aperture Radar (ISAR) imaging techniques are used to generate the images presented in this paper. The measurements are performed with stationary antennas, in a quasi-monostatic configuration, and a rotating target. The scattered energy is detected then recorded and processed. The coherent sum of the signal received is used to generate a two dimensional image of the target which represents the spatial location of scattering centers. Prior to forming the image, wavelet analysis is applied to produce images allowing for visualization of various scattering phenomena.

The results presented in this paper experimentally demonstrate that wavelet multi-resolution analysis can be used to examine wave medium interactions in radar

images. Chapter 2 begins with background material including an overview of ISAR imaging techniques and signal processing methods for reducing window effects and implementing range gates. It concludes with background information on wavelet analysis and the application of multi-resolution frequency domain analysis to radar imaging. The methodology is outlined in Chapter 4. The experimental method and test procedures are explained as well as the data processing procedure. Scattering measurements are performed for several test cases consisting of metallic targets to experimentally demonstrate the method for implementing a sliding range gate through multi-resolution analysis. The data processing is performed using routines written using Mathematica from Wolfram Research and the associated package, Wavelet Explorer in which the wavelet transform is implemented through the pyramid algorithm. The results of the study are presented and discussed in Chapter 5. These results demonstrate that the sliding range gate implemented through frequency domain multi-resolution analysis provides a method for analyzing scattering phenomena in radar images. Finally, Chapter 6 contains conclusions and ideas for future work.

CHAPTER 2

BACKGROUND

This chapter contains an overview of ISAR imaging techniques in addition to signal processing methods for reduction of window effects and implementation of range gating. A brief discussion of wavelet analysis provides background information followed with methodology for multi-resolution frequency domain analysis.

2.1 ISAR Imaging

Basic field theory defines the electric field vector as a function of space and time according to

$$\bar{E} = \bar{E}_o \cdot \exp(-j(\bar{k} \cdot \bar{R} - \omega t)) \quad (2-1)$$

for a positional vector \bar{R} where \bar{k} is the wave vector defining the direction of incidence. The incident field, \bar{E}^i , is reflected, transmitted or absorbed, based on the characteristics of the target [3]. The scattered field is a function of frequency, angle of incidence, polarization, as well as, geometry and material properties of the target. Assuming the target is a perfect conductor, all of the energy is scattered.

The complex scattered electric field $\bar{E}^s(k_x, k_y)$ in k-space coordinates (k_x, k_y) is given by

$$\bar{E}^s(k_x, k_y) = \int_{-\infty}^{\infty} \int_{-\infty}^{\infty} \Gamma(x, y) \cdot \exp(-j \cdot 2\pi(k_x x + k_y y)) dx dy \quad (2-2)$$

where $\Gamma(x, y)$ is the object reflectivity density function. The above equation defines the relationship that exists between the scattered field and the object reflectivity. Since the scattered far field is obtained directly from measurements the reflectivity density function

$$\Gamma(x, y) = \int_{-\infty}^{\infty} \int_{-\infty}^{\infty} \bar{E}^s(k_x, k_y) \cdot \exp(j \cdot 2\pi(k_x x + k_y y)) dk_x dk_y \quad (2-3)$$

is determined by taking the inverse Fourier transform. Linear system theory can be applied due to the fact that electromagnetic fields are linear and therefore obey superposition [1].

An ISAR image is created from measurements performed with a stationary radar irradiating a rotating target. To form an image of the target, the scattered fields from the different aspect angles are coherently summed. ISAR utilizes target motion to generate a synthetic aperture for resolution in azimuth while the downrange resolution is determined by the radar frequency bandwidth. The down-range resolution, Δr_d , is given by

$$\Delta r_d = \frac{c}{2B} \quad (2-4)$$

where B is the frequency bandwidth and c is the speed of light. The cross range resolution, Δr_c , is given by

$$\Delta r_c = \frac{\lambda}{2\Delta\theta} \quad (2-5)$$

where λ is the wavelength and $\Delta\theta$ is the total angular aperture [4].

To produce a focused image, the data is polar formatted and re-sampled to a rectangular grid prior to performing the 2-D inverse fast Fourier transform (IFFT). The magnitude of the scattered field, as a function of frequency and angle is shown in Figure 2.1(a). In k-space, Figure 2.1(b), the scattered field is on a polar grid, where $2f/c$ is the polar radial parameter and θ is the polar angle parameter corresponding to the measurement aspect angle. Following the k-space interpolation the 2-D IFFT transforms the data to the time (spatial) domain. For an electromagnetic wave traveling in air, time, t , and distance, d , are related by the speed of light, $c = d/t$. Therefore, the spatial representation of the target reflectivity can be determined. The spatial domain representation is shown in Figure 2.1(c).

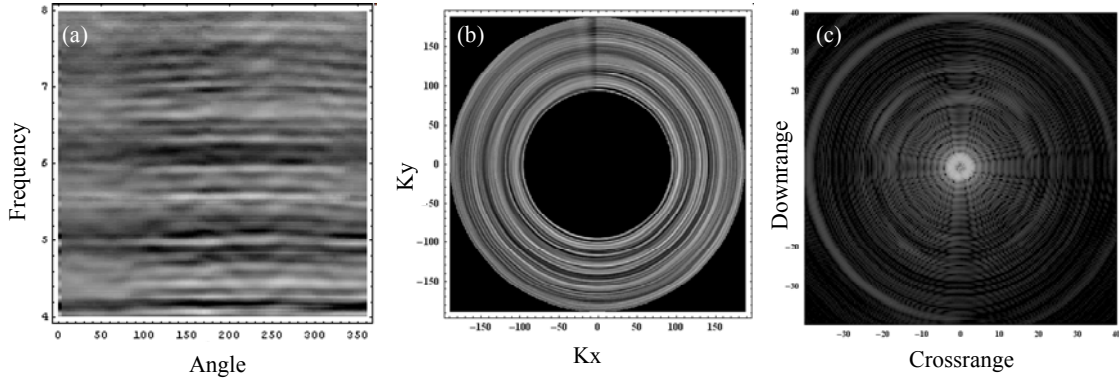


Figure 2.1 Data Format (a) Frequency Domain, (b) K-Space Domain, and (c) Spatial Domain

The image intensity corresponds to the object's reflectivity at a given spatial location designated by the down range and cross range axes. The resulting image provides a means to determine the spatial location of scattering sources. ISAR imaging techniques are used to generate all of the images presented in this paper.

2.2 Window Effects

Window effects appear as artifacts in the image due to the finite extent of the data. As a result of the periodic assumption of the Fourier transform and the discontinuity at the band edges, erroneous frequency content corrupts the time domain response. Sharp transitions result in high sidelobes. The measured signal in k-space is band limited, which is equivalent to multiplication of the frequency domain signal by a rectangular window. Multiplication in the spectral domain corresponds to convolution of the time domain signal with a $\sin(t)/t$ function. Therefore, the truncation of the frequency domain signal results in leakage related to the sidelobe characteristics of the $\sin(t)/t$ function [5]. The width of the main lobe and the level of the side lobes can be controlled by the type of windowing function applied to the data.

In the case of ISAR imaging, the 2-D IFFT is performed on the k-space data. In this case, the bandwidth limitations correspond to an annular shaped windowing function. To demonstrate, an ISAR image is created for the unit amplitude annular window shown in Figure 2.2(a). The image in Figure 2.2(b) illustrates the artifacts that occur in the 2-D ISAR image due to the windowing effect. The spatial domain response of the annular window appears as a central peak surrounded by circular sidelobes [6].

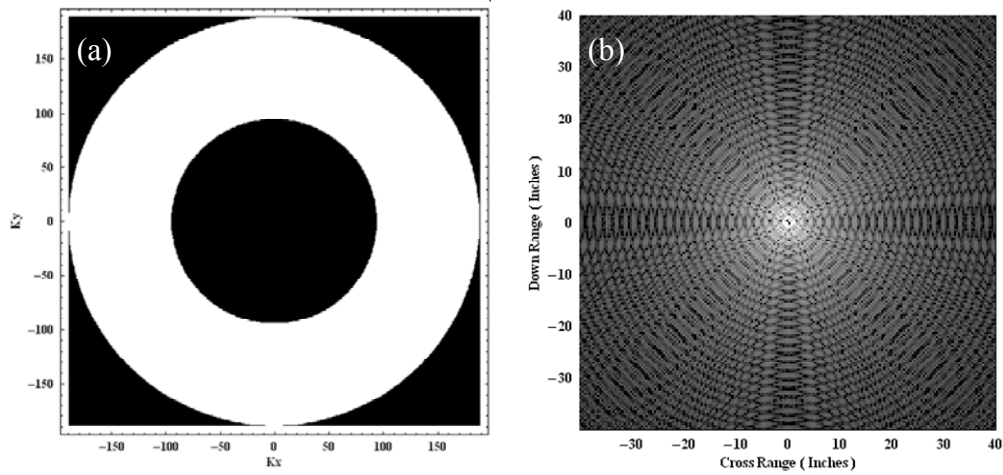


Figure 2.2 Window Effects (a) K-Space and (b) Spatial Domain

Techniques to minimize the effects of spectral leakage in ISAR images seek to control the width of the mainlobe and the relative levels of the sidelobes. They include use of traditional weighting functions as well as spectral estimation and sidelobe reduction algorithms. A traditional method for minimizing window effects is through application of tapered weighting functions. By convolving the signal with a tapered window, the sidelobe structure can be modified or minimized. Application of a symmetric tapered window, such as a hanning window, smooths the boundary discontinuities resulting in lower sidelobes [7]. There is a trade off with resolution since the window tends to broaden the mainlobe. Since the weighting function effectively decreases the bandwidth there is a smoothing of the spatial domain response. This loss in resolution leads to the reduction in ability to resolve closely spaced scatters.

More complex spectral estimation techniques such as the maximum entropy method and autoregression are used to suppress sidelobes through extrapolation of the data. Other sidelobe reduction techniques include spatially variant apodization, the

minimum variance method and others. An overview of these techniques can be found in [8].

2.3 Range Gating

Radar cross section measurement has unwanted signals present from various sources [9]. Range (time) gates are used to sample the received scattered signal at a specified time. The gate may be implemented through software or hardware methods. Hardware gating adds complexity and cost to the system. Software gating provides a more cost effective solution in addition to added functionality which allows for changing the position and type of gate [10]. Range gating is used to spatially isolate scattering sources and to reject scattering occurring outside the region of interest as depicted in Figure 2.3. Measured frequency domain data is time gated through

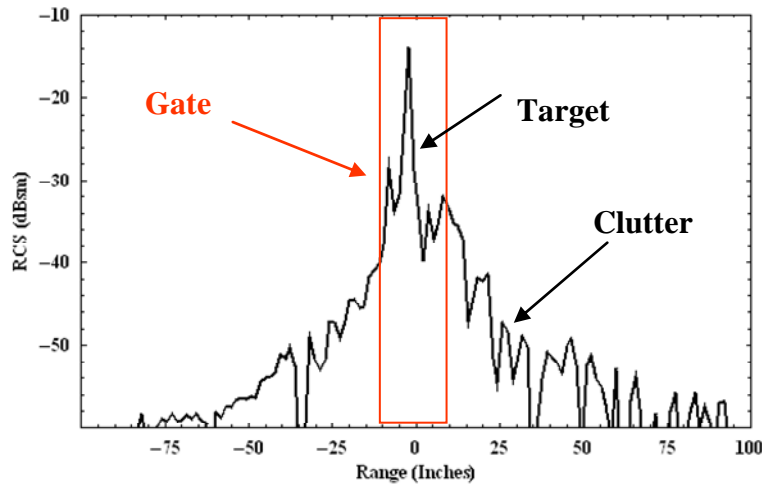


Figure 2.3 Range Gating for Clutter Rejection

application of a temporal band-pass filter. The filtered time domain data is transformed back to the frequency domain to obtain time gated frequency domain data. The

placement and width of the gate can be specified for selection of scattering sources of interest. To minimize sidelobes resulting from time gating, tapered windows are used. There is a trade off with resolution since the window tends to broaden the mainlobe. In this study, time gating is implemented through multi-resolution frequency domain analysis.

2.4 Wavelets

Wavelet analysis is similar to Fourier analysis in that they both expand time functions in terms of basis functions. The fundamental difference is that the finite characteristics of the wavelet make it ideal for detecting short duration variations in signals. In literal terms, a wavelet is a small wave. A wavelet must meet the following conditions; it must be localized in time and exhibit oscillations in time. It contains finite energy, therefore when the wavelet, $\psi(t)$, is integrated over time, as in the equation below, it yields zero net area.

$$\int_{-\infty}^{\infty} \psi(t) dt = 0 \quad (2-6)$$

There are many types of wavelets. The Daubechies wavelet is the simplest member of a class of scaling functions developed by Daubechies [11] and is used for the investigations in this study. Through dilation and translation of the analyzing (or mother wavelet) a family of wavelets is formed for use in representing and characterizing functions. The power of the wavelet is found from its ability to analyze signals through use of time frequency localization.

The discrete wavelet transform is implemented in Mathematica Wavelet Explorer V1.2.2 through the pyramid algorithm developed by Mallat [12]. With this method, decompositions are performed with a fast wavelet transform through convolution. The discrete approximation $a_j(t)$, where j is the resolution level, of the original sampled signal $f(t)$ is given by the inner product of the scaling function ϕ_{jk} with the signal $f(t)$. The details of the decomposition $d_{j-1}(t)$ are given by

$$d_{j-1}(t) = \sum_k d_k^{j-1} \psi_{j-1,k}(t) \quad (2-7)$$

where the coefficient d_k^{j-1} is given by the inner product of the wavelet $\psi_{j-1,k}$ and the signal $f(t)$. Similarly, the approximation coefficients a_k^{j-1} are formed through the inner product of the scaling function and the signal. Therefore, the approximation of the signal at resolution level j is defined as

$$a_j(t) = a_{j-1}(t) + d_{j-1}(t) = \sum_k a_k^{j-1} \phi_{j-1,k}(t) + \sum_k d_k^{j-1} \psi_{j-1,k}(t) \quad (2-8)$$

which means that the approximation of the original signal at each resolution level can be found by summing the approximation and detail from the previous level. Following multi-resolutions analysis, the original signal can be recovered through summation of the approximation at level j to the details j through n where n corresponds to the number of decompositions and $a_j(t)$, in above equation is the discrete approximation of the original signal.

$$f(t) = a_j(t) + \sum_{k=j}^n d_k(t) \quad (2-9)$$

The results of the derivation of the explicit expressions for the approximation and detail coefficients is shown here. The approximation coefficients are calculated according to

$$a_k^{j-1} = \langle \phi_{j-1,k}, f \rangle = \sum_l h_{l-2k} \langle \phi_{jl}, f \rangle \quad (2-10)$$

which corresponds to the inner product of the scaling function, $\phi_{j-1,k}$, and the signal which is equivalent to the time domain convolution of the low pass filter h and the signal. Similarly, the detail coefficients

$$d_k^{j-1} = \langle \psi_{j-1,k}, f \rangle = \sum_l g_{l-2k} \langle \phi_{jl}, f \rangle \quad (2-11)$$

are formed from the inner product of the wavelet $\psi_{j-1,k}$ and the signal which is equivalent to the time domain convolution of the high pass filter g and the signal.

The two above equations correspond to the equations for the pyramid algorithm. A relationship exists between the wavelet transform and filter bank theory [13]. The decomposition and reconstruction of the signal is easily demonstrated when compared with a filter bank. The decomposition of the signal is equivalent to passing the signal through a low pass, $\tilde{H}(\omega)$, and high pass, $\tilde{G}(\omega)$, filter pair as shown in Figure 2.4. The output of each filter is then down-sampled by two resulting in the coefficients a_k^{j-1} and d_k^{j-1} . To reconstruct the signal, the coefficients are up-sampled and passed through the conjugate low pass and high pass filter pair, as shown in Figure 2.5, which corresponds to the inverse wavelet transform applied to the coefficients to obtain the approximation and detail resolutions of the original signal.

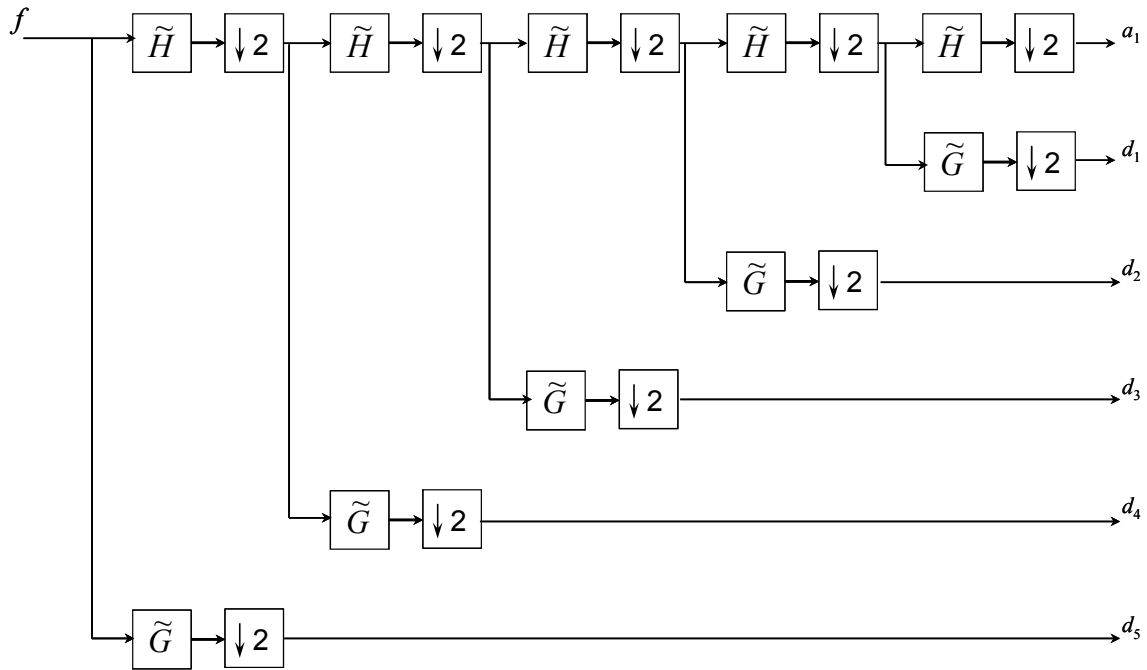


Figure 2.4 Block Diagram of a 5-Level Orthogonal Wavelet Decomposition

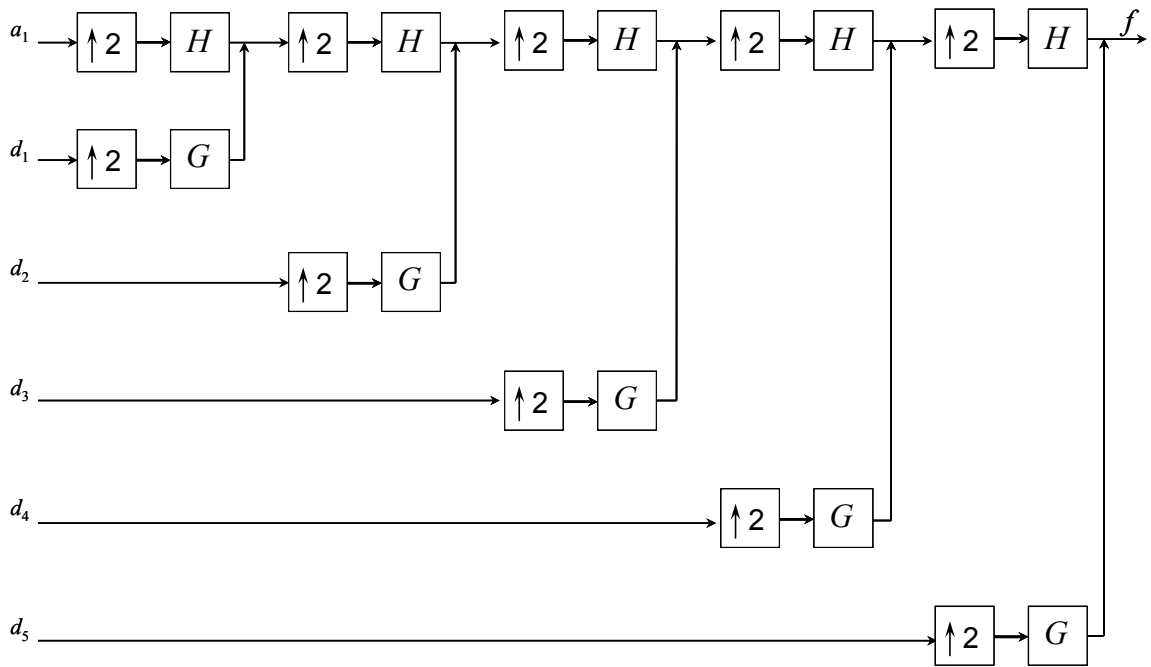


Figure 2.5 Block Diagram of a 5-Level Orthogonal Wavelet Reconstruction

An equivalent methodology is followed for the technique utilized in this study. A frequency domain signal is filtered and down sampled. The coefficients obtained correspond to resolutions of the spectral domain scattered field. The reconstruction is performed as before to obtain the frequency domain approximation or detail of the original signal. The following section describes in detail how multi-resolution wavelet analysis can be used, in the frequency domain, to extract wave medium interaction phenomena in radar images. Through multi-resolution frequency domain analysis, range gating is possible. It is shown that, sliding range gates are easily implemented in the frequency domain prior to the spatial domain transform.

2.5 Multi-Resolution Frequency Domain Analysis

2.5.1 Implementation

Typically wavelet analysis is applied to time domain signals to obtain time localized frequency content. For this application, the discrete wavelet transform is applied directly to the frequency domain signal. A single transform provides information at multiple spatial locations. The wavelet properties which allow for localization of frequency content in time, correspond to a segmentation of the time axis which results in time gates of increasing width with increasing time as shown in Figure 2.6. The width of the gate is governed by the temporal domain resolution (Δt) of the data. The example shown in Figure 2.6 depicts six resolutions of a signal where the lower resolutions correspond to early time and higher resolutions correspond to later time. In the spatial domain, lower resolutions correspond to gates positioned spatially near the reference location while higher resolutions are further from the reference. The

reference in this case is the rotational center of the measurement setup, corresponding to the origin in the radar image.

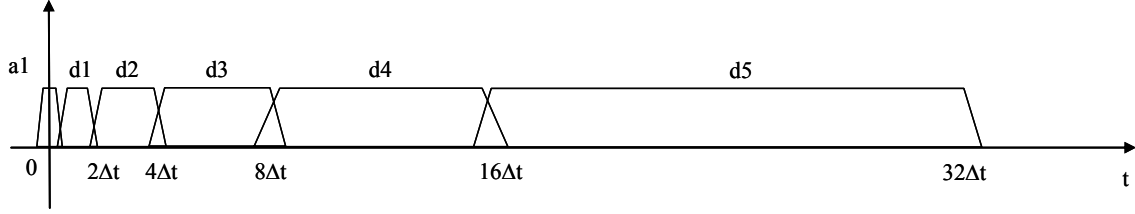


Figure 2.6 Segmentation of Time Domain

Since the wavelet transform performs dyadic decimation of the signal, the number of data points should consist of a power of two in order to maximize the number of decompositions. This allows for the smallest possible time gate limited only by the time domain resolution of the data. In order to separate two targets, the gate must be narrow enough such that the gate does not encompass both targets. It is also desirable to keep the gate small relative to the target in order to observe incremental changes in the scattered field over time.

To implement multi-resolution frequency domain analysis, the wavelet transform is applied directly to the complex scattered field. Following decomposition and reconstruction, the complete scattered field

$$\bar{E}^s = \bar{E}_{a_1}^s + \sum_{k=1}^n \bar{E}_{d_k}^s \quad (2-12)$$

at each look angle is recovered through summation of the coarsest approximation $\bar{E}_{a_1}^s$ and the details $\bar{E}_{d_k}^s$ where k corresponds to the specific detail and n is the number of decompositions. Note that each approximation and detail is a complex value obtained

from the real and imaginary parts obtained from the multi-resolution analysis. Below is a list of the nomenclature used to represent the results of the multi-resolution analysis with respect to the scattered field.

\bar{E}^s	Complex Valued Scattered Field A function of frequency f and aspect angle (ϕ, θ)
ϕ	Azimuth Angle
θ	Elevation Angle (Constant in this case.)
$\bar{E}_{a_j}^s$	Approx of Complex Valued Scattered Field $\bar{E}_{a_j}^s = \text{Re}[\bar{E}_{a_j}^s] + j \text{Im}[\bar{E}_{a_j}^s]$
$\bar{E}_{d_k}^s$	Detail of Complex Valued Scattered Field $\bar{E}_{d_k}^s = \text{Re}[\bar{E}_{d_k}^s] + j \text{Im}[\bar{E}_{d_k}^s]$
$\text{Re}[\bar{E}^s]$	Real Part of Complex Valued Scattered Field
$\text{Im}[\bar{E}^s]$	Imaginary Part of Complex Valued Scattered Field

The diagram in Figure 2.7 demonstrates how the measured signal is decomposed, reconstructed and finally processed to generate the ISAR image.

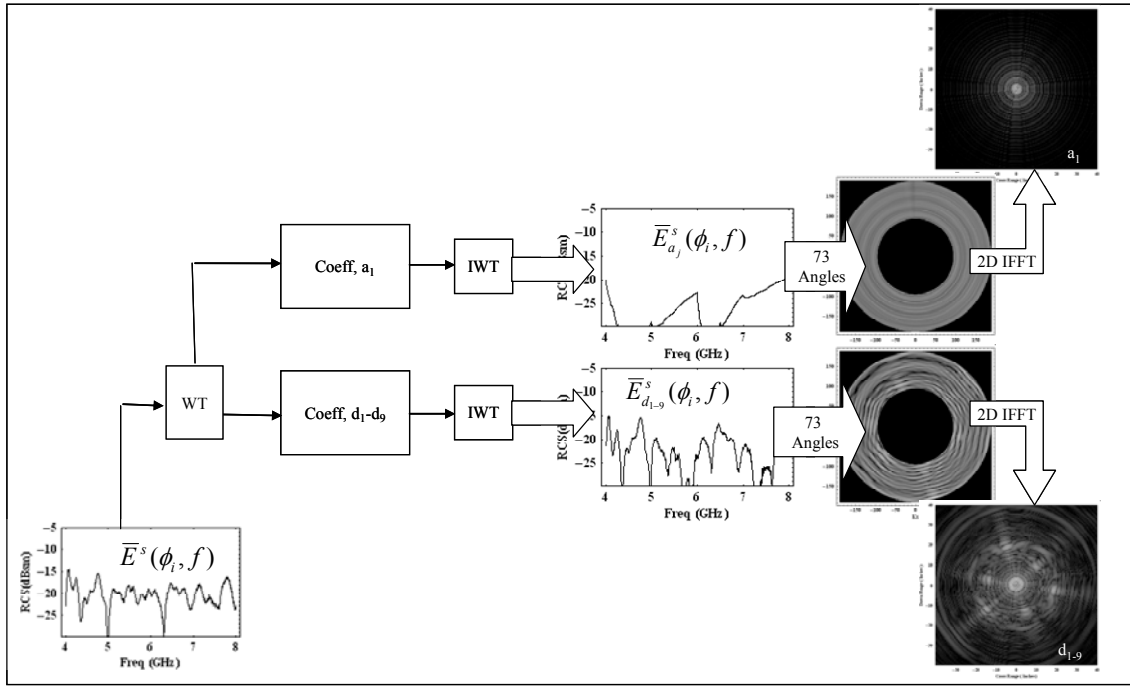


Figure 2.7 Multi-Resolution Frequency Domain Analysis

2.5.2 Physical Meaning

Spectral domain multi-resolution analysis corresponds to gating in the spatial (temporal) domain. In order to demonstrate the gating properties of the wavelet transform, wavelet analysis is applied to the scattered electric field from a metal sphere. In this particular case, a Daubechies 4 (Daub4) wavelet was used and eight decompositions were performed. The wavelet decomposition is performed on the measured data for a single look angle ($\phi = 0$) and selected coefficients are reconstructed prior to transforming to the time domain. The time domain responses of the multi-resolution analysis are shown in Figure 2.8 along with the complete time domain response. The gated time domain responses are displayed with increasing resolution from left to right. The time domain response of approximation 3,

$\bar{E}_{a_3}^s = \bar{E}_{a_1}^s + \bar{E}_{d_1}^s + \bar{E}_{d_2}^s$, is shown in Figure 2.8 (a) with the response of details 3, 4, and 5, $\bar{E}_{d_3}^s + \bar{E}_{d_4}^s + \bar{E}_{d_5}^s$, shown in Figure 2.8(b) and finally details 6 and 7, $\bar{E}_{d_6}^s + \bar{E}_{d_7}^s$ in Figure 2.8(c).

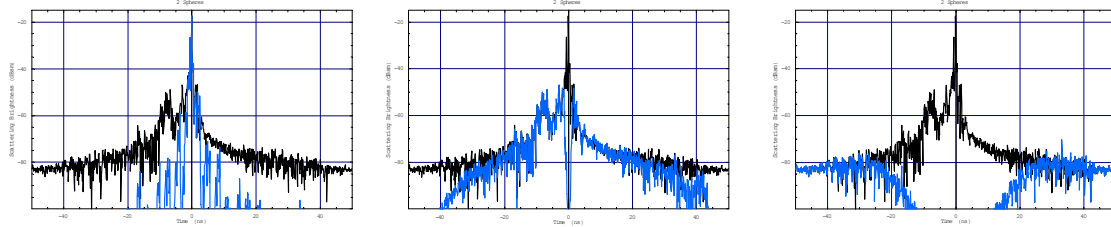


Figure 2.8 Time Domain Response at a Single Look Angle (a) Approximation 3, (b) Details 3-5 and (c) Details 6-7 using Daub4 with 8 Decompositions

The results demonstrate the time gating property of wavelet multi-resolution analysis when applied to a frequency domain signal. The time domain response is displayed from ± 50 ns or roughly ± 50 feet. Selection of $\bar{E}_{a_3}^s$, Figure 2.8(a), corresponds to a 2 ns wide gate centered at $t = 0 \cdot ns$. Selection of this resolution effectively removes the clutter by positioning the gate such that the response from the metal sphere is selected. Increasing resolutions relate to selection of later time events or spatial locations further from the measurement reference location as shown in Figure 2.8 (b) and (c). These fundamental techniques are used to apply range gating to radar images. An extension of this method provides flexibility by allowing for selective positioning of the gate. Application of a phase shift to the frequency domain scattered field effectively slides the gate in time.

Figure 2.9 contains the time domain scattering response for two metal spheres. The lowest wavelet resolution is shown in blue corresponding to a time gate centered at

$t = 0 \cdot ns$. Through application of a phase shift to the scattered field, prior to transforming to the time domain, the signal is shifted and the gate remains stationary.

For example, Figure 2.10 contains the time domain response, corresponding to

$$\bar{E}^s \cdot \exp(-j2\pi \cdot f \cdot t_0) \quad (2-13)$$

where $t_0 = 1.0 \cdot ns$.

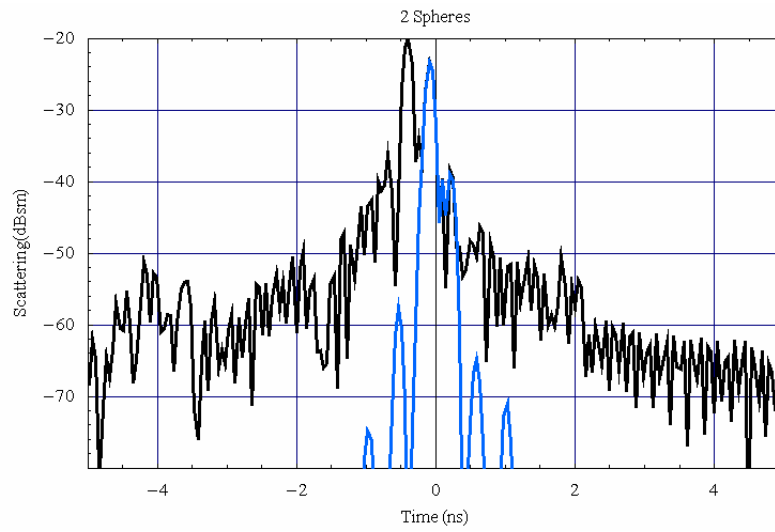


Figure 2.9 Time Domain Response, a_1 , prior to phase shift

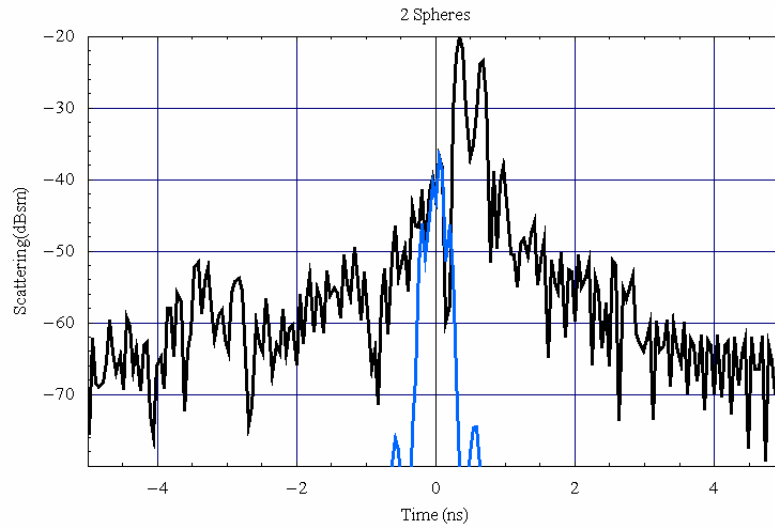


Figure 2.10 Time domain response, a_1 , for $t_0 = 1.0 \cdot ns$

Note that the signal is shifted to later time and the gate remains stationary resulting in selection of earlier time responses. Further description of the specific implementation is contained in the following chapter.

CHAPTER 3

METHODOLOGY

A detailed description of the methodology used to demonstrate the removal of window effects and the implementation of a sliding range gate is contained in this chapter. A brief description of the measurement technique is given followed by the data processing steps applied to the calibrated scattered far field.

3.1 Data Collection

Scattering measurements were performed for several target configurations to demonstrate that properties of wavelet multi-resolution analysis for separation of wave medium interaction phenomena. In all test cases, metallic targets were measured in a quasi-monostatic configuration. The test configurations are listed below in Table 3.1 and the corresponding pictures are in Figure 3.1.

Table 3.1 Experimental Test Cases

Test Case	Target
1	4" Diameter Metal Sphere
2	Metal Triangular Target
3	Sphere and Triangle (dz=7")
4	Sphere and Triangle (dz=11")

The sphere and triangle were initially measured independently to characterize the scattering response of each target. After measuring the targets separately, the two

objects were measured together with the sphere located on a seven inch foam column above the triangle centered on the z-axis or axis of rotation as shown in Figure 3.1 (c). This test was then repeated with the sphere placed on an eleven inch foam column to determine if the difference in separation between the two targets could be detected.

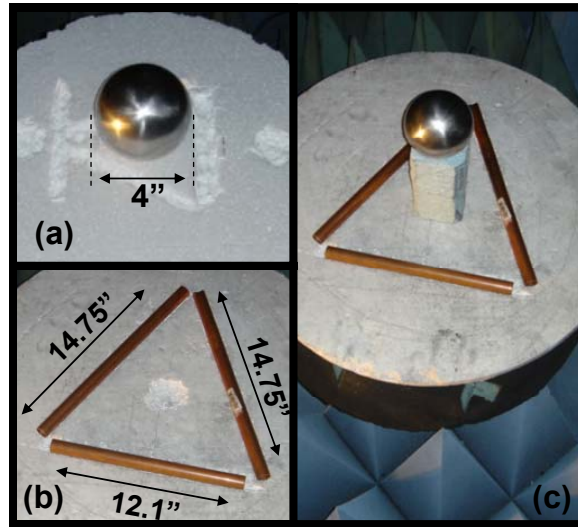


Figure 3.1 RCS Measurement Test Units (a) Sphere, (b) Triangular and (c) Sphere & Triangular Targets

All of the tests were performed in the University of Texas at Arlington (UTA) anechoic chamber according to the test parameters outlined in Table 3.2. The measurement chamber is equipped with a HP 8510C network analyzer and utilizes Labview data acquisition software. For the purposes of this study, only a single polarization was evaluated. Vertical polarization is transmitted and received. Two conical dual polarized broadband horns are utilized for the tests. The antennas are located side by side, as shown in Figure 3.2, and therefore are in a quasi-monostatic configuration.

Table 3.2 Test Parameters

Parameter	Value	Increment	# Points
Frequency	4-8 GHz	5 MHz	801
Azimuth Angle	0-360°	5°	73
Polarization	VV	n/a	n/a
Reference Angle	$\theta=60^\circ$	n/a	n/a

The transmit and receive antennas are positioned in the farfield with a 60 degree angle of incidence, as measured from the z-axis. Frequency is swept from 4-8 GHz in 5 MHz increments resulting in 801 frequency points at each look angle. Figure 3.3 specifies the incidence angle and axis of rotation for a typical test. The azimuth angle ϕ was stepped from 0-360 degrees in five degree increments.

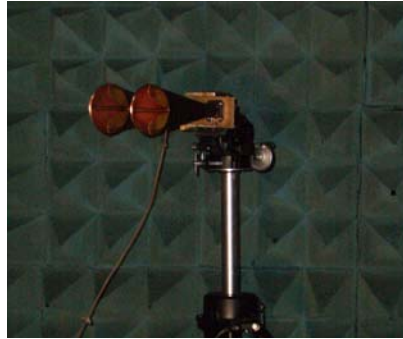


Figure 3.2 Broadband Dual Polarization Conical Horns

Standard calibration techniques are used to correct the measured data as outlined in [3]. Background measurements are performed of the empty chamber and of the chamber containing target supports to obtain the reference and target backgrounds, respectively. A four inch diameter metal sphere is used as the calibration reference standard. Theoretical scattering for the reference sphere was calculated using the program in Appendix E. Following calibration, the acquired data was analyzed as described in the following section.

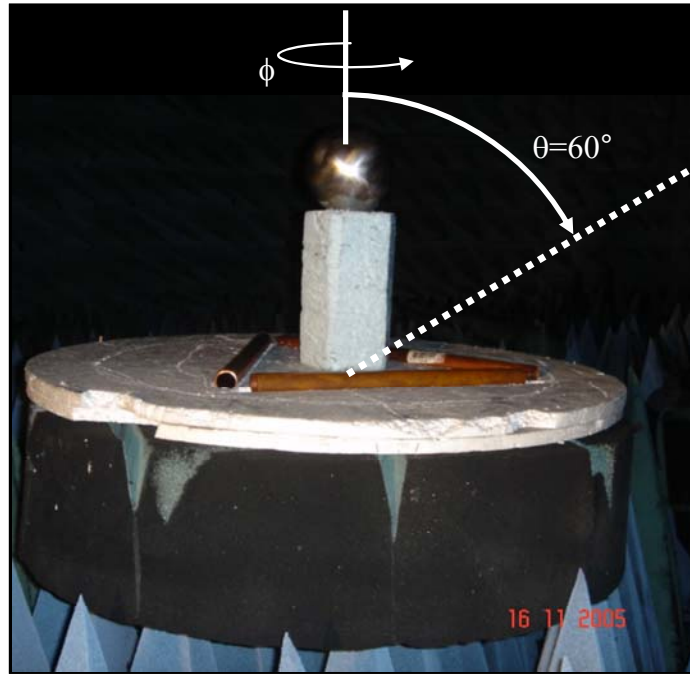


Figure 3.3 RCS Measurement Setup

3.2 Data Processing

This section describes the processing carried out on the set of received signals to obtain an image of backscattered microwave energy for individual resolutions. Each of the processing steps is performed on a single frequency sweep, which corresponds to a single look angle. The complex signal is first calibrated according to standard methods and interpolated. The window effects are removed and range gates are implemented utilizing multi-resolution techniques. The final step of generating the ISAR image is performed on the two dimensional multi-resolution data. In the following section, each step is mathematically described and spatial domain plots, obtained through the IFFT of the spectral domain data, are presented to provide a visual description of the techniques.

Mathematica Student Version 5.2 with Wavelet Explorer Version 1.2.2 is used for all processing steps. The flow chart in Figure 3.4 contains the data analysis steps. All of the processing steps are performed in the frequency domain.

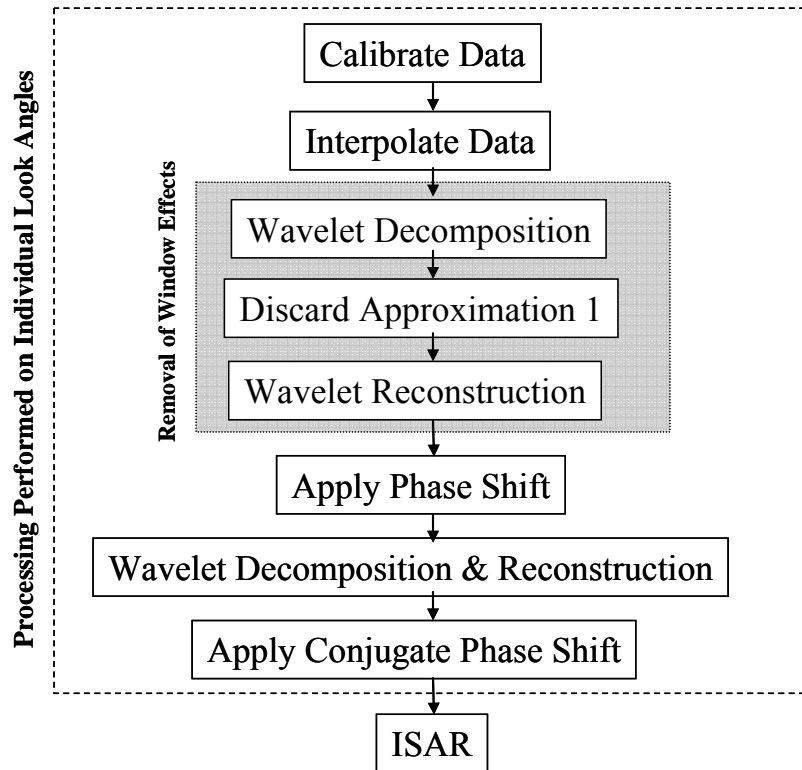


Figure 3.4 Multi-Resolution ISAR Imaging Flow Chart

Each data set contains scattered electric fields as a function of frequency and aspect angle obtained by irradiating a rotating target with a stationary antenna. Standard calibration and background subtraction techniques are used. After the data is calibrated, interpolation is performed, on a single frequency sweep corresponding to a single look angle. The interpolation is needed to increase the number of data points to a power of two to maximize the number of multi-resolution decompositions. As a result of the interpolation, the frequency domain resolution increases which corresponds to an

increase in the time domain range. Interpolation of the data to 1024 data points was selected since it is the next higher power of two. Since the frequency resolution relates to the range according to

$$t_{\min/\max} = \pm \frac{(n \cdot \Delta t)}{2} \quad (3-1)$$

and since the frequency bandwidth BW determines the time domain resolution and is calculated according to

$$\Delta t = \frac{1}{2BW} = \frac{1}{2n \cdot \Delta f} \quad (3-2)$$

a further increase in the number of points is not required. For example, in this case, considering the measured 5 MHz frequency increment, a range of +/-50 ns is obtained and for the interpolated 3.9 MHz frequency increment a range of +/-64 ns is obtained.

The 4 GHz bandwidth used for the measurements results in a time step of $0.125 \cdot ns$, which defines the widths of the time gates as described in Table 3.3. A Daubechies 2 (Daub2) wavelet was selected for all of the data analysis presented. The corresponding gate widths, for data length of 1024 points, with nine decompositions, are shown for each resolution in Table 3.3. For these test cases, the lower resolutions provide the most meaningful information. The targets are fully contained within a two nanosecond gate therefore resolutions a_1 and d_{1-3} are of the greatest interest.

Table 3.3 Time Gate Widths for Daub2, 9 Decompositions, $\Delta t=0.125$ ns, 1024 points

Time Gates, 4-8 GHz, 1024 points Daub2 Wavelet, 9 Decompositions		
<i>Resolution</i>	<i>Gate Width (ns)</i>	<i>Gate min and max (ns)</i>
a1	0.125	0 to +/-0.125
d1	0.125	+/-0.125 to +/-0.25
d2	0.250	+/-0.25 to +/-0.5
d3	0.500	+/-0.5 to +/-1.0
d4	1.000	+/-1.0 to +/-2.0
d5	2.000	+/-2.0 to +/-4.0
d6	4.000	+/-4.0 to +/-8.0
d7	8.000	+/-8.0 to +/-16.0
d8	16.000	+/-16.0 to +/-32.0
d9	32.000	+/-32.0 to +/-64.0

The corresponding spatial gates for each wavelet resolution are contained in Table 3.4. Note that the 0.125 ns time step corresponds to 1.5 inches of range resolution.

Table 3.4 Spatial Gate Widths for Daub2, 9 Decompositions, $\Delta s=1.5$ ", 1024 points

Spatial Gates, 4-8 GHz, 1024 points Daub2 Wavelet, 9 Decompositions		
<i>Resolution</i>	<i>Gate Width (inches)</i>	<i>Gate min and max (inches)</i>
a1	1.5	0 to +/-1.5
d1	1.5	+/-1.5 to +/-3.0
d2	3.0	+/-3.0 to +/-5.9
d3	5.9	+/-5.9 to +/-11.8
d4	11.8	+/-11.8 to +/-23.6
d5	23.6	+/-23.6 to +/-47.2
d6	47.2	+/-47.2 to +/-94.4
d7	94.4	+/-94.4 to +/-188.8
d8	188.8	+/-188.8 to +/-377.7
d9	377.7	+/-377.7 to +/-755.4

3.2.1 Removal of Windowing Effects

Radar images contain windowing effects due to the finite nature of the data. As demonstrated in Chapter 2, the k-space representation of a constant valued real function

for all frequencies and aspect angles produces artifacts in the ISAR image, as shown in Figure 2.2. Multi-resolution frequency domain analysis provides an efficient means of removing these effects. In order to remove the windowing effects, the wavelet transform is performed separately on the real and imaginary parts of the complex scattered field for each look angle. The real and imaginary components are then reconstructed, via the inverse wavelet transform, with the coefficients for the lowest approximation $\bar{E}_{a_1}^s$ set to zero. By removing the lowest approximation, $\bar{E}_{a_1}^s$, the scattered field with the window removed,

$$\bar{E}_{wr}^s = \sum_{k=1}^n \bar{E}_{d_k}^s \quad (3-3)$$

is now represented only by the summation of the details, $\bar{E}_{d_k}^s$. Following removal of window effects, the sliding gate is implemented with an applied phase shift as described in the following section.

3.2.2 Sliding Gate Implementation

A phase shift is applied to the spectral domain scattered field for each look angle according to

$$\bar{E}_{wr_sh}^s(f) = \bar{E}_{wr}^s(f) \cdot \exp(-j \cdot 2\pi \cdot f \cdot t_0). \quad (3-4)$$

The complex valued scattered field with the window effects removed, \bar{E}_{wr}^s , is multiplied by an exponential with $-j \cdot 2\pi \cdot f \cdot t_0$ as the argument for a fixed time shift t_0 as a function of frequency f to obtain the phase shifted field $\bar{E}_{wr_sh}^s(f)$. The phase shifted signal is decomposed for each look angle and the individual terms are reconstructed. In

the following example nine decompositions were performed therefore the signal is decomposed into the lowest approximation $\bar{E}_{wr_sh_{a1}}^s$ and details $\bar{E}_{wr_sh_{d_k}}^s$, for $k = 1, 2, \dots, 8$. To demonstrate the effects of the phase shift, Figure 3.5 contains two spatial domain plots with the complete spatial domain response of the signal along with the spatial domain response of $\bar{E}_{wr_sh_{a1}}^s$ in bold for $t_0 = 0.5 \cdot ns$, Figure 3.5(a) and $t_0 = 1.5 \cdot ns$ Figure 3.5(b). Note that as the spatial domain response is shifted to an earlier time, the gate remains fixed, centered at $t = 0 \cdot ns$. Since the gate corresponding to a_1 remains fixed and the signal moves to an earlier time, later time scattering responses are selected.

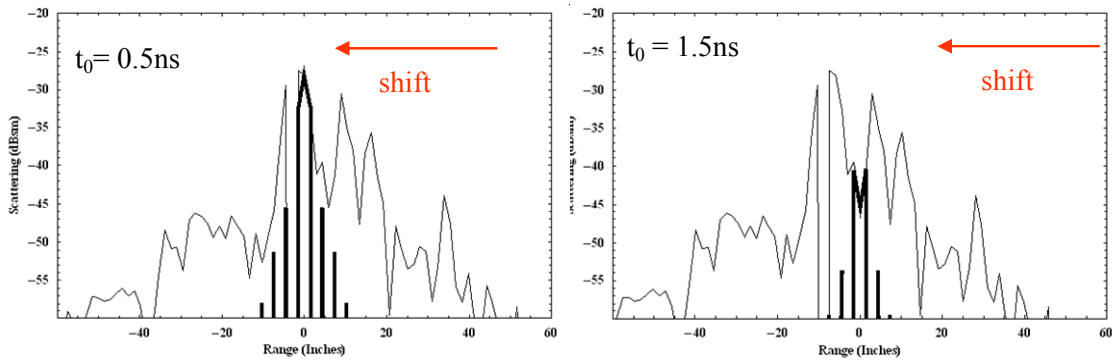


Figure 3.5 Sliding Gate Spatial Domain Response with a_1 (bold) for Initial Shift (a) $t_0 = 0.5ns$ and (b) $t_0 = 1.5ns$

After the individual resolutions are reconstructed, a conjugate phase shift is applied to correct each of the resolutions for the initial applied phase shift. The conjugate phase shift is applied to each resolution for each look angle according to

$$\bar{E}_{wr_sh2}^s = \bar{E}_{wr_sh}^s \exp(-j \cdot 2\pi \cdot f \cdot (-t_0)). \quad (3-5)$$

Example spatial domain plot for $\overline{E}_{wr_sh\,a_1}^s$ are shown in bold in Figure 3.6 (a) and (b) with the spatial domain response for the original signal prior to phase shifting.

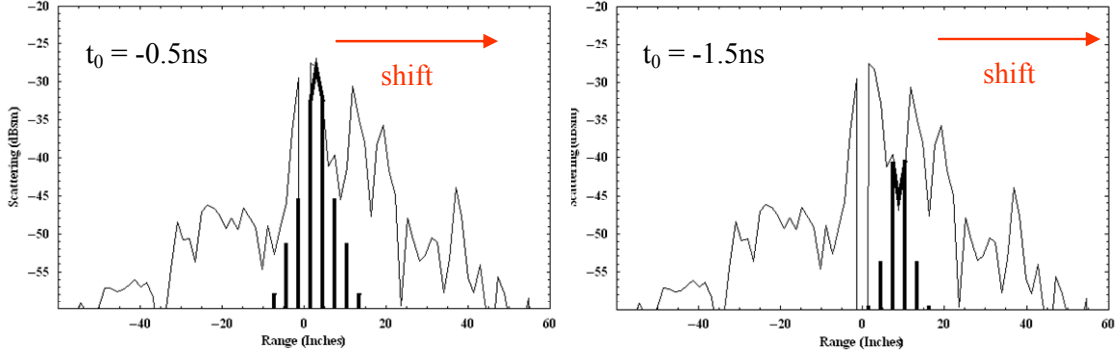


Figure 3.6 Sliding Gate Spatial Domain Response with a_1 (bold) for Conjugate Shift (a) $t_0 = -0.5ns$ and (b) $t_0 = -1.5ns$

Note that the original shift has been corrected and the time gates are now centered at $t = 0.5 \cdot ns$ and $t = 1.5 \cdot ns$ in Figure 3.6 (a) and (b), respectively. Therefore, through multi-resolution techniques, a sliding gate is implemented. The final step is to generate the ISAR images for each resolution to examine the scattering phenomena corresponding to different instances in time.

3.2.3 ISAR Images

Standard ISAR techniques, as described in Chapter 2, are used to generate the images. Polar reformatting is performed and the k-space values are interpolated to a Cartesian grid prior to performing the 2-D IFFT. Example images are shown in Figure 3.7. The images shown in Figure 3.7 correspond to the scattering response from the four inch metal sphere shown in Figure 3.1(a) following multi-resolution analysis. Only the lowest six resolutions are shown since they contain the most meaningful information. Referring to Table 3.3 and Table 3.4, the lower six resolutions have a

range of ± 4 ns or ± 4 feet. In the spatial domain, the targets are fully enclosed within a two foot square area therefore gating a region of ± 4 ns is more than sufficient to observe the scattering response for this study. As can be observed in the images, the higher resolutions correspond to later time scattering phenomena. A more in depth discussion of these and other results are contained in the following chapter.

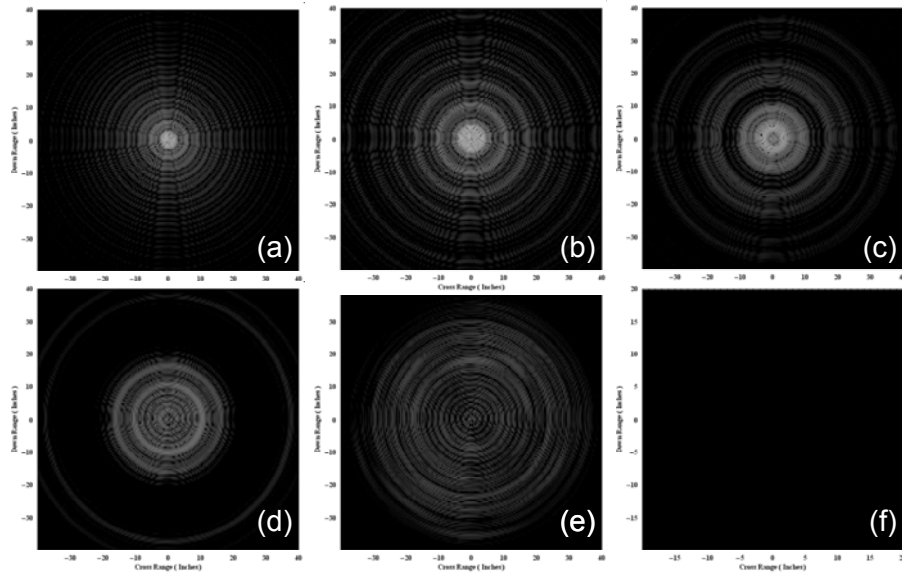


Figure 3.7 Multi-Resolution ISAR Images Metal Sphere (a) Approximation 1 and (b-f) Details 1-5

CHAPTER 4

EXPERIMENTAL RESULTS AND DISCUSSION

To demonstrate time-frequency analysis techniques for reducing artifacts in radar images, several experiments were performed. The results indicate that further analysis of scattering phenomena in radar images is possible through implementation of sliding range (time) gates. This chapter contains the results from the four experimental test cases described in the previous chapter. Images are shown with window effects removed demonstrating a reduction in the artifacts induced by the finite nature of the data. Images constructed using the results of the multi-resolution analysis are also shown demonstrating the ability of multi-resolution frequency domain analysis to extract wave medium interaction phenomena. In all four test cases, a Daub2 wavelet was used for processing and nine decompositions were carried out. The individual reconstruction of the lower six resolutions are used to generate the ISAR images. Finally, d_1 corresponding to a 0.125 ns time gate, is used to generate images resulting from incrementally sliding the gate. The images provide a means to analyze how the wave medium interactions change with time.

4.1 Removal of Window Effects

To demonstrate removal of the window effects from the ISAR image, the scattered far field from test case 4 was decomposed and reconstructed for each aspect angle. Nine decompositions were performed and the signal was reconstructed with the

lowest approximation set to zero. The removal of window effects is easily implemented by discarding the lowest approximation for each aspect angle. To demonstrate, the images corresponding to the lowest five resolutions are shown in Figure 4.1. The resolutions, which are a function of frequency and aspect angle, are interpolated and mapped to the spatial frequency domain prior to performing the IFFT to generate the ISAR images shown. The spatial domain representation for the lowest approximation, far left image in Figure 4.1, duplicates the spatial domain response obtained in Chapter 2 for the annular shaped window.

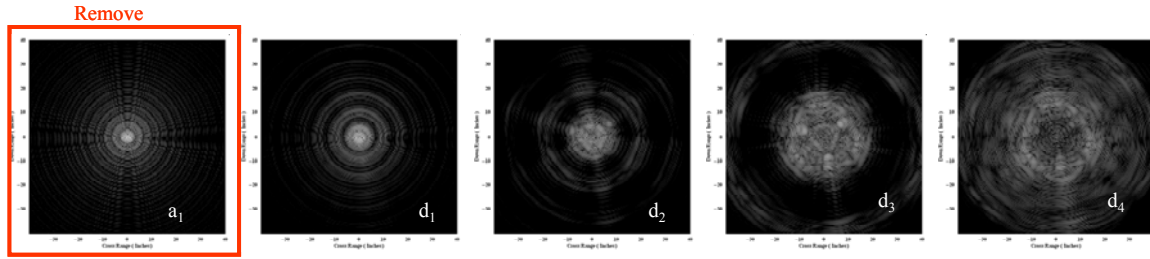


Figure 4.1 Multi-Resolution ISAR Images Prior to Removal of Window Effects

Removal of the window effects results in reduction of artifacts in the image. The initial ISAR image shown in Figure 4.2(a) is formed from the data prior to multi-resolution processing. Figure 4.2(b) contains the image of the lowest approximation representative of the window effects. Finally, an image, Figure 4.2(c), is created from the scattered far field data following removal of the lowest approximation, corresponding to details 1-9.

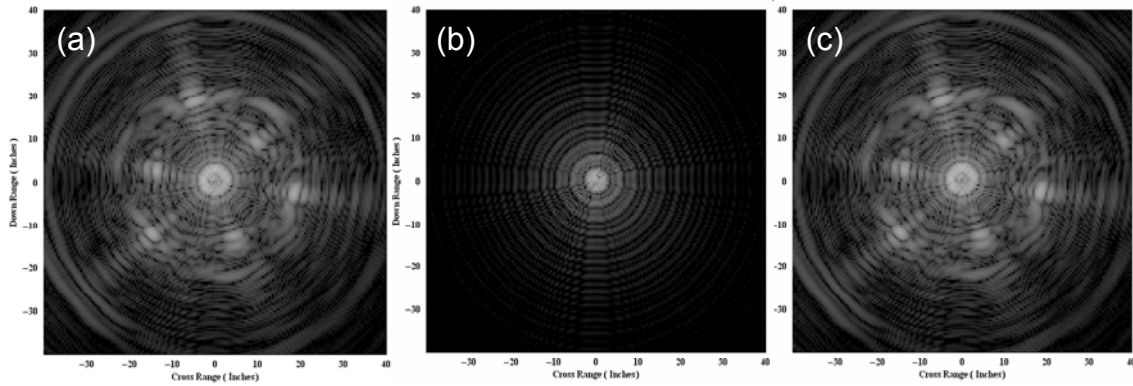


Figure 4.2 ISAR Images (a) Initial, (b) Approximation 1 and (b) Details 1-9

Since the processing takes place in the frequency domain, this method provides an efficient means to remove window effects. Unless otherwise stated, all of the ISAR images in the remainder of the text have window effects removed.

4.2 Physical Meaning of Resolutions

For each test case, multi-resolution analysis was performed utilizing the method described in Chapter 3 with a second order Daubechies filter. The maximum number of decompositions was performed and the reconstructed waveforms from the lowest six resolutions were used to generate ISAR images. The results shown in this section verify the findings in [2] that multi-resolution analysis of spectral domain scattered field data allows for selection of scattering phenomena at earlier or later times.

These results relate the resolutions obtained from wavelet multi-resolution analysis to the observed wave medium interactions apparent in the radar images. The images presented in this section correspond to the time gates outlined in Table 3.3. These images also provide a comparison to those corresponding to a sliding time gate

presented later in the chapter. Results from all four test cases are included, followed by discussion. The initial case is for the metal sphere.

4.2.1 Scattering Phenomena from a Metal Sphere

The four-inch diameter metal sphere shown in Figure 3.1(a) is used for test case 1. The sphere circumference is between four and nine wavelengths therefore, the sphere produces a resonant scattering response [3]. Over the measured frequency bandwidth, significant changes in phase occur resulting in a creeping wave response. By combining multi-resolution analysis with radar imaging, it is possible to analyze the changes in the fields with respect to time.

The ISAR image generated using standard techniques, shown in Figure 4.3, exhibits the characteristic response of a metal sphere. The image contains a specular scattering response occurring at each look angle. The one dimensional down range image for a single look angle contains a peak at a range of two inches due to the specular scattering from the sphere. An identical response is expected for all aspect angles due to the rotational symmetry of the target. The ring visible in the image has a two inch radius as does the sphere. The grayscale levels in the image range from -90 to -20 dBsm from black to white respectively. The one dimensional cross range image (Figure 4.4) is a cut through the down range origin. The peaks located at ± 2 inches correspond to the two inch radius of the sphere as in the ISAR image.

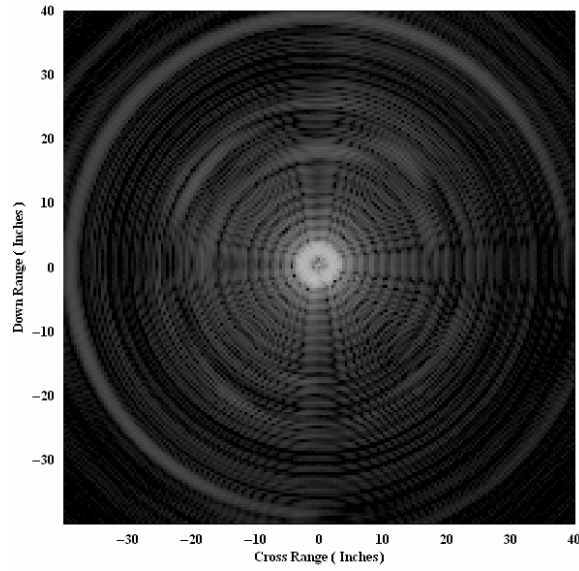


Figure 4.3 ISAR Image 4" Metal Sphere

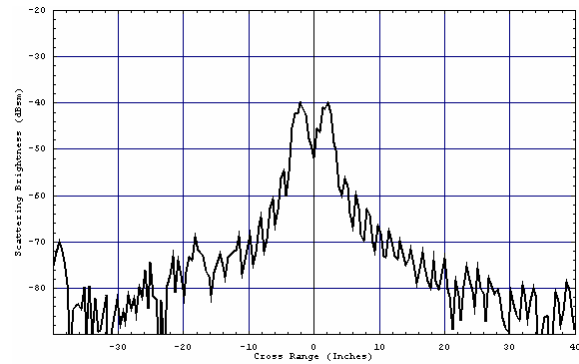


Figure 4.4 Cross Range Image ($downrange = 0$) 4" Metal Sphere

In order to examine the results of multi-resolution frequency domain analysis, images for the lower six resolutions were created. The scattered far field data was processed with nine decompositions but only the lower resolutions are of interest since the target is contained within a one foot square region. Figure 4.5 illustrates the locations of the time gates for a_1 and d_{1-5} . The measurement reference (center of rotation) corresponds to $t = 0 \cdot ns$. The earliest time gate, corresponding to a_1 is

centered at $t = 0 \cdot ns$ and is $0.125 \cdot ns$ wide. The latest time gate, d_5 centered at $t = 3 \cdot ns$ and is $2 \cdot ns$ wide. The multi-resolution ISAR images corresponding to a_1 and d_{1-5} are shown in Figure 4.6. The images are ordered from coarsest to finest resolutions (or from early to later time) from left to right and top to bottom.

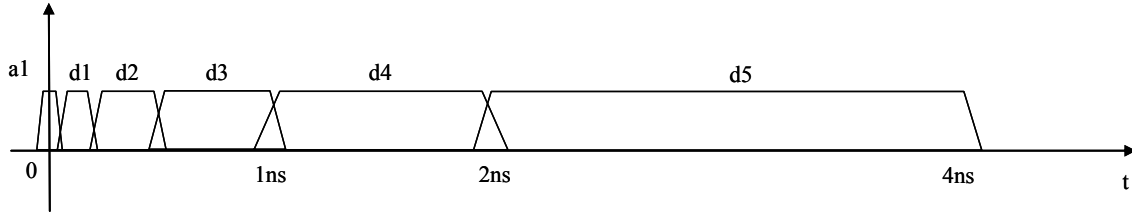


Figure 4.5 Time Domain Representation Approximation 1 and Details 1-5

The images corresponding to the lowest resolutions a_1 and d_1 , Figure 4.6(a) and (b), contain the highest intensity scattering levels. This is expected because the sphere is physically contained within these time gates. The image for a_1 , Figure 4.6(a), has a peak value of at -40 dBsm and matches peak levels obtained in the original image of Figure 4.3. With increasing resolution, the intensity levels are expected to decrease since the higher resolutions relate to scattering phenomena occurring at later arrival times. This is confirmed through analysis of the images in Figure 4.6. It is apparent that with increasing resolution, the scattered fields spread and decay until in Figure 4.6(f) no scattering response is visible in the image.

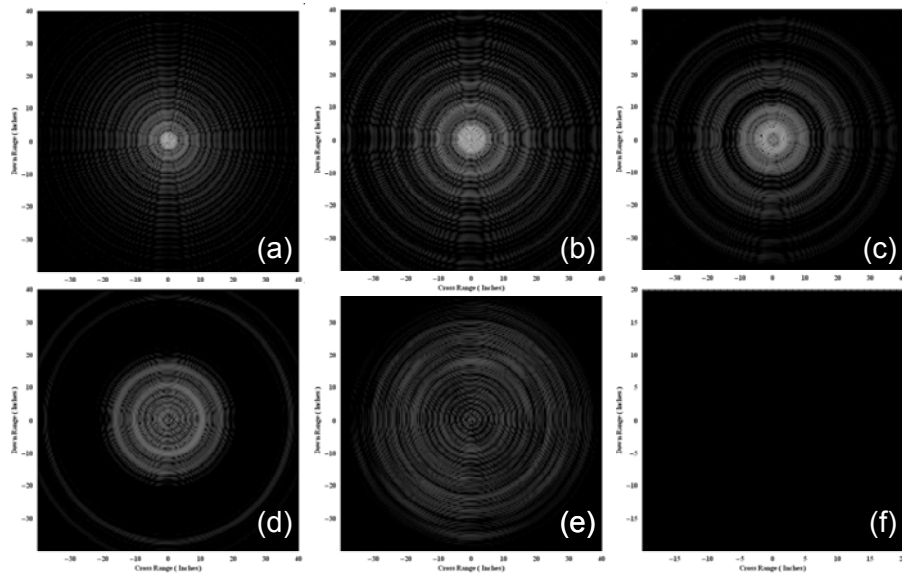


Figure 4.6 Multi-Resolution ISAR Images Metal Sphere (a) Approximation 1 and (b-f) Details 1-5

Since the metal sphere has an isotropic response, a second target was selected to evaluate whether time frequency analysis can be used to distinguish other types of wave medium interaction phenomena.

4.2.2 Scattering Phenomena from a Triangular Target

The second test case consisted of three 0.8 inch diameter metal rods arranged in a triangular shape as shown in Figure 3.1(b). Two of the rods are 14.75 inches long and the third is 12.1 inches long. The triangle is positioned such that the direction of incidence at zero degrees is approximately normal to the 12-inch rod. The scattering geometry for the triangular target is shown in Figure 4.7. The scattering at $\phi = 0$ degrees is a specular response since the incident field is normal to the 12-inch rod. For incidence angles of 114 and 246 degrees a specular response is also expected since the incident field is normal to the rods, as depicted in Figure 4.7. For incidence angles 42,

180 and 318 degrees a scattering response due to diffraction is expected since at these angles the fields are incident at the ends of the adjoining rods.

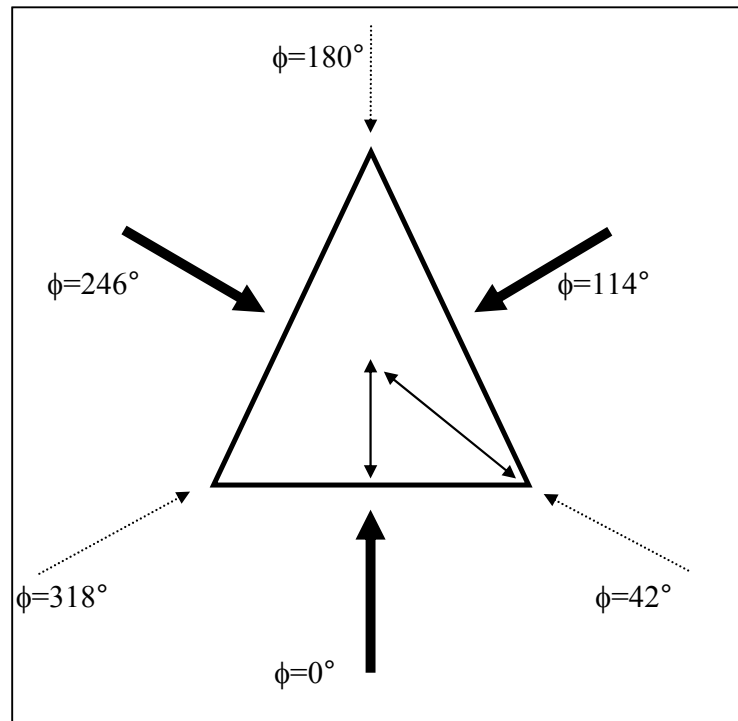


Figure 4.7 Scattering Geometry for Metal Triangular Target

Even though clutter is apparent in the image, the shape of the triangle is evident in the ISAR image shown in Figure 4.8. Specular scattering appears at the normal to each rod appearing to spread outward from the origin. Diffraction occurs at the ends of the rods and is also visible in the image. The grayscale image displayed has minimum and maximum levels from -90 to -20 dBsm. A one-dimensional cross range image shown in Figure 4.9 corresponds to a slice through the down range origin. The distance between the two rods is approximately nine inches, which agrees with the location of the peak scattering levels visible in Figure 4.9.

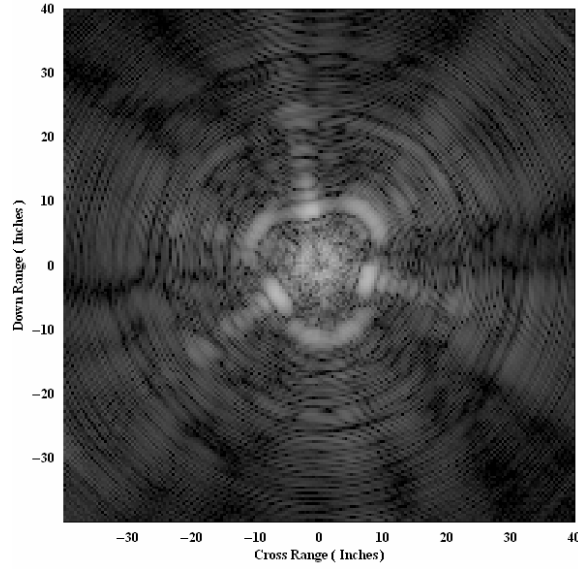


Figure 4.8 ISAR Image Metal Triangular Target

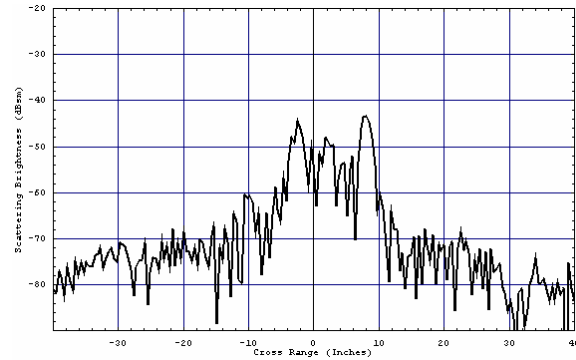


Figure 4.9 Cross Range Image ($downrange = 0$) of Metal Triangular Target

The results of the multi-resolution analysis are organized as before and are shown in Figure 4.10. The specular scattering, at incidence angles normal to the rods, appears in the lower resolutions, Figure 4.10(a) and (b). The outline of the triangle in addition to the diffraction from the ends of the rods first becomes visible in Figure 4.10(c). This image corresponds to d_2 or to a 0.25 ns wide gate centered at 0.375 ns. The results agree with the physical characteristics of the target. Relative to the origin, the distance to the side of a rod is shorter than the distance to the ends as shown in

Figure 4.7. Therefore, the specular scattering from the sides is expected to occur at an earlier time than the diffraction from the ends. The images in Figure 4.10(d) and (e) are representative of later time therefore the field intensity appears further away from the target. For the highest resolution shown in Figure 4.10(f) the fields are at a sufficiently low level throughout the image indicating the decay of energy.

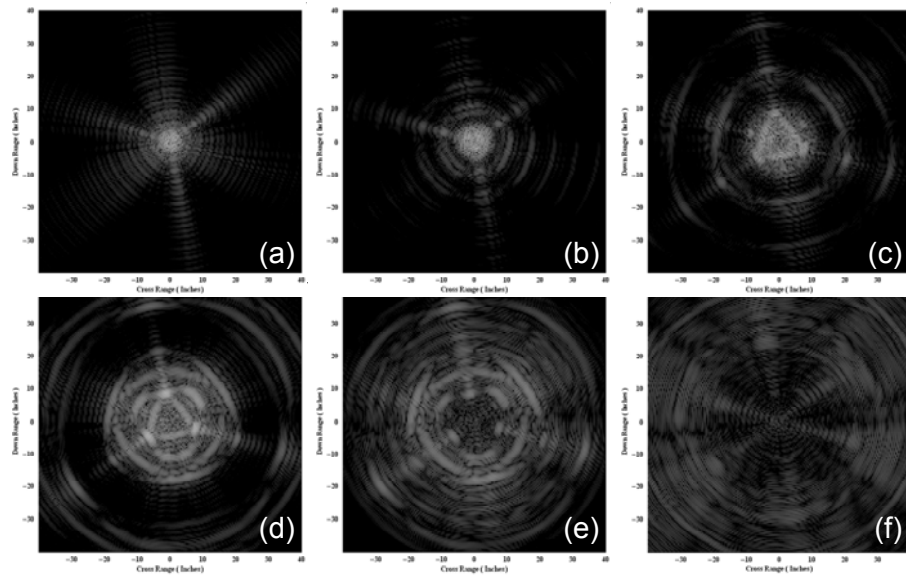


Figure 4.10 Multi-Resolution ISAR Images Triangular Target (a) Approximation 1 and (b-f) Details 1-5

The results from the triangular target provide additional substantiation to the relationship between the wavelet resolutions and specific time gates. This also provides further validation of the time-frequency analysis technique for clutter reduction in the ISAR images. Now that the two targets have been characterized individually, further analysis is performed utilizing both targets. The goal is to evaluate the use of wavelet analysis to distinguish scattering phenomena from multiple targets.

4.2.3 Scattering Phenomena from Multiple Targets

Measurements for the triangular target and a metal sphere were performed in the configuration shown in Figure 3.1(c). The sphere and triangle were tested in two configurations with different separation between the two objects. In both cases, the sphere was placed on a foam column centered on the axis of rotation. Initially the sphere was positioned on a foam column seven inches above the triangle. For the final test case, the sphere was placed on an eleven inch foam column. As with the previous test cases, the scattered field was used to generate images.

The initial image was generated for test case 3 and is shown in Figure 4.11. The triangle appears larger in the image due to the fact that the triangle is seven inches below the reference position. The sphere is also visible in the image and shows up centered at the origin as expected. The grayscale image ranges from -90 to -20 dBsm. In Figure 4.12, the response from the sphere appears at ± 2 inches in cross range while a smaller response, at approximately 14 inches in cross range, appears due to the triangular target. Comparison of Figure 4.12 with Figure 4.9 reveals that the scattering from the triangle appears approximately seven inches further from the origin due to the separation between the two targets.

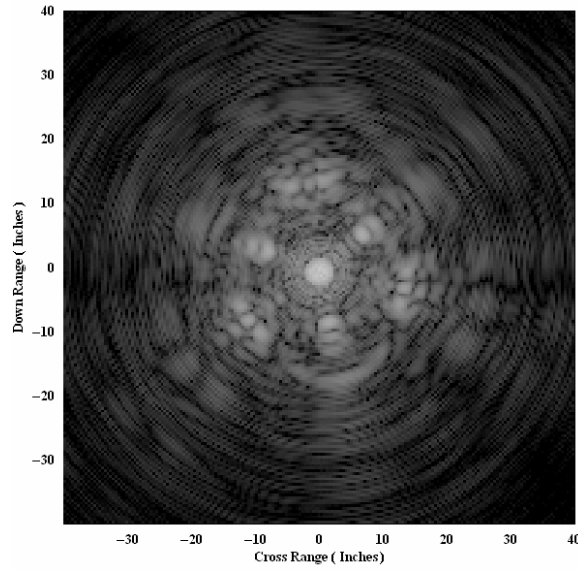


Figure 4.11 ISAR Image Sphere and Triangle Targets, $dz = 7''$

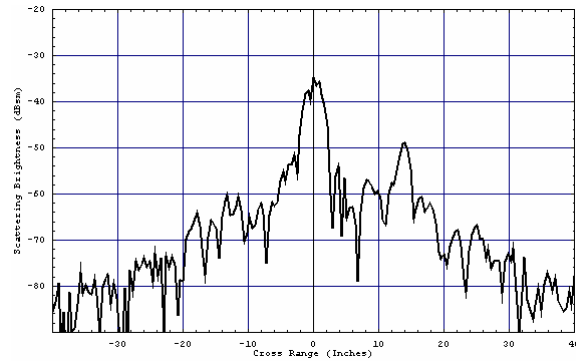


Figure 4.12 Cross Range Image ($downrange = 0$) of Sphere and Triangle, $dz = 7''$

Figure 4.13 contains the images resulting from the multi-resolution analysis. The scattering from the sphere is visible in the lower resolutions, Figure 4.13(a) and (b). This is expected since the sphere is located at the reference location and is completely encompassed by the time gates corresponding to a_1 and d_1 with the combined width of these two gates corresponding to ± 0.25 ns or ± 3 inches. The scattering response from the triangle first becomes evident in the image corresponding to d_2 , Figure 4.13(c). Since the distance from the origin to the side of the triangle is roughly six

inches, it is expected that the specular scattering from the triangle would be visible in the image corresponding to d_2 . This gate ranges from 0.25 to 0.5 ns (3 to 6 inches) which corresponds to the location of the triangle. In Figure 4.13(d) and (e) the scattering response of the triangle is still visible as the fields appear to spread outward from the reference position. The fields have decayed significantly for the highest resolution shown in Figure 4.13(f). The scattering levels are minimal in the image corresponding to d_5 , Figure 4.13(f), since the scattering response is greater than two feet from the reference position.

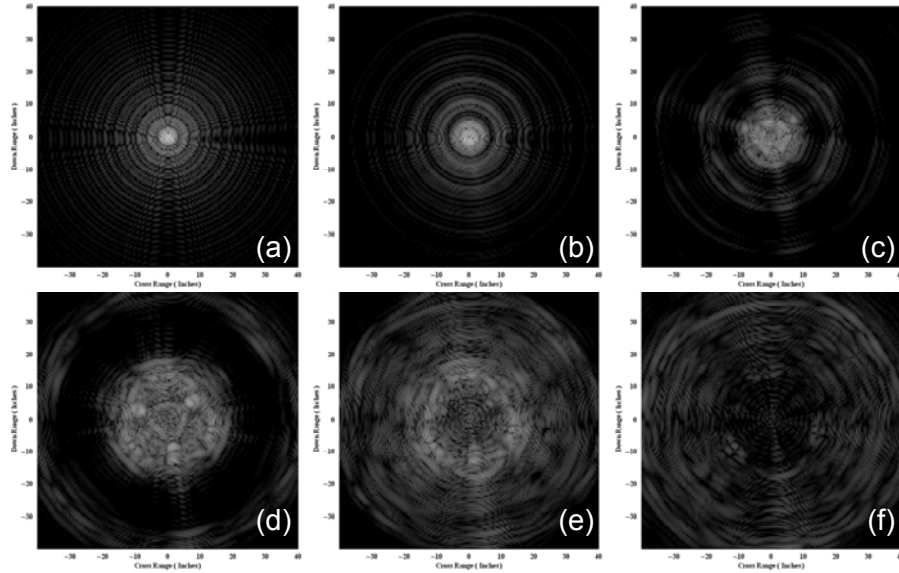


Figure 4.13 Multi-Resolution ISAR Images Metal Sphere & Triangle $dz = 7''$
(a) Approximation 1 and (b-f) Details 1-5

Test case 3 validates that scattering phenomena from multiple metallic targets can be imaged separately using wavelet analysis techniques. While complete separation of the coupling between the two targets is not possible, the wave medium interactions that are characteristic of the individual targets are distinguishable for different

resolutions. The objective of the final test case is to utilize multi-resolution techniques to detect the change in the separation distance between the two targets.

The final test case is identical to the previous except now the sphere is positioned on an 11 inch foam column. The initial ISAR image is shown in Figure 4.14. As before, the four inch diameter metal sphere appears in the image as a ring with a two inch radius clearly defined and centered at the origin. Scattering phenomena characteristic of the triangular target appears further from the origin due to the increased offset from the reference position. Figure 4.15 contains the cross range image through the down range origin. The response from the sphere is visible as two peaks on either side of the origin with levels of -40 dBsm. The specular scattering response from one of the rods forming the triangle is visible at 19 inches in cross range. Comparison with Figure 4.12 indicates that the scattering response from the triangle has moved an additional four inches away from the reference position due to the increased height of the sphere.

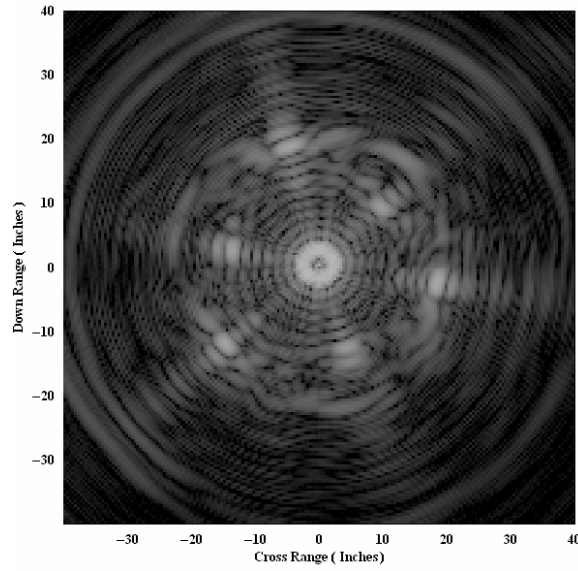


Figure 4.14 ISAR Image Sphere and Triangle Targets, $dz = 11''$

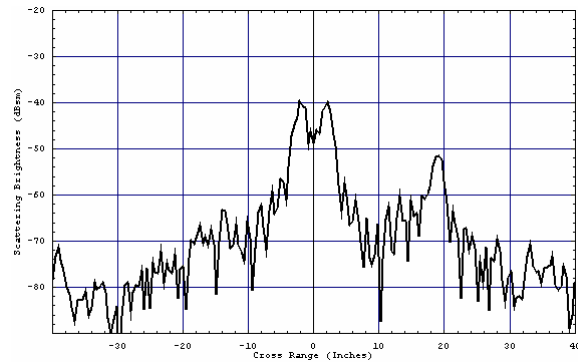


Figure 4.15 Cross Range Image ($downrange = 0$) of Sphere and Triangle, $dz = 11''$

The resulting images from the wavelet multi-resolution analysis are shown in Figure 4.16. As in test case 3, the response from the sphere appears in the lower resolutions, Figure 4.16 (a) and (b). Comparison of the images corresponding to d_2 for both cases (Figure 4.13(c) and Figure 4.16(c)) reveals that only the scattering from the sphere is evident in test case 4. For test case 3, the initial specular scattering response

from the triangle is visible in the image due to the smaller separation between the two targets. This confirms that, through analysis of the multi-resolution images, it is possible to detect the difference in separation between two targets. For the images corresponding to the higher resolutions there is little difference between test case 3 and test case 4. Since the higher resolutions correspond to wider gates, the increase in separation is relatively small therefore virtually undetected.

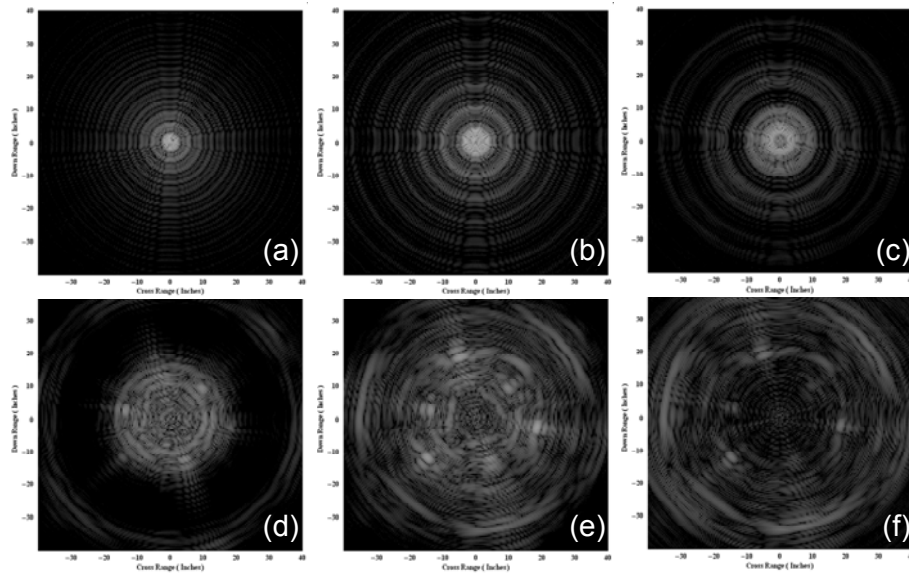


Figure 4.16 Multi-Resolution ISAR Images Metal Sphere & Triangle $dz = 11''$
(a) Approximation 1 and (b-f) Details 1-5

These experiments provide additional support to the findings in [2] that the lower resolutions correspond to early times and that higher resolutions correspond to later times. The individual resolutions have been used to remove clutter in radar images as well as to separate and analyze the wave medium interaction phenomena from individual targets. The final section investigates the application of a sliding range gate for full analysis of the radar images.

4.3 Implementation of Sliding Gate

In this section, a sliding range gate is implemented through application of a phase shift to the spectral domain scattered field prior to wavelet analysis. For each test case, a phase shift resulting from shifting the gate 0.5 ns is evaluated. For the test cases with multiple targets, additional processing was performed with a 1.25 ns shift for further comparison. Finally, the effect of progressive phase shifts applied to a single resolution is presented to demonstrate the ability to visualize the evolution of the fields in the images with respect to time and space.

4.3.1 Gated Scattering Response Metal Sphere

A phase shift resulting from a 0.5 ns time shift is applied to the metal sphere data prior to wavelet decomposition. The conjugate phase shift applied after the reconstruction of the individual coefficients corrects the signal prior to forming multi-resolution images as described in Chapter 3. The multi-resolution images corresponding to sliding the gate 0.5 ns (6 inches) are shown in Figure 4.17. Comparison of these images to the initial images in Figure 4.6 reveal a change in the response. It is not surprising that there is no change at the highest resolution Figure 4.17(f) since this resolution represents responses which are greater than two nanoseconds from the reference location therefore the response is expected to be nearly zero. The lower resolutions that relate to early time responses show more clearly defined rings suspected to result from the oscillations set up due to the interaction between the specular and creeping waves.

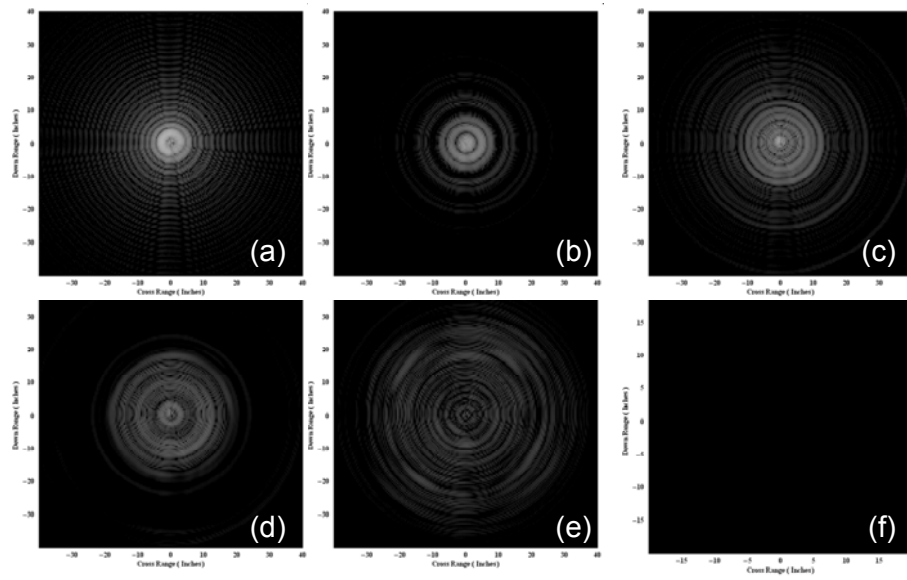


Figure 4.17 Multi-Resolution ISAR Images Metal Sphere $t_0 = 0.5ns$ (a) Approximation 1 and (b-f) Details 1-5

In order to visualize the change in the scattering response over time, analysis of a single resolution with incremental shifts was performed. Based on the target size, d_1 was selected since it represents a gate with width of 0.125 ns or 1.5", which, for this study, is small enough to visualize changes in the radar images. Through an applied phase shift, an effective sliding time gate with width of 0.125 ns is implemented. The time domain representation of the gate corresponding to d_1 prior to shifting, for $t_0 = 0 \cdot ns$, is shown in Figure 4.18. Figure 4.19 demonstrates how the progressive phase shifts are applied to the spectral domain signal for each aspect angle resulting in shifting the gate incrementally in 0.125 ns steps.

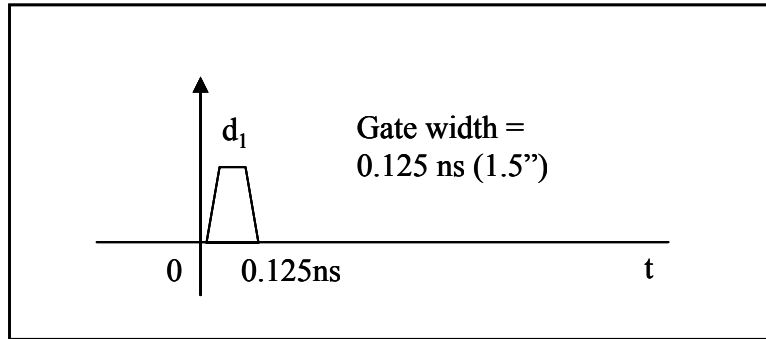


Figure 4.18 Time Domain Representation of Gating

The series of images generated, Figure 4.20, are normalized to the peak value for $t_0 = 0 \cdot ns$. They are displayed on a scale ranging from -25 to 0 dBsm. The down range and cross range axes range from ± 20 inches. The first image (upper left corner) corresponds to the initial gate, for $t_0 = 0 \cdot ns$. The time gate is progressively shifted with time increments of $\Delta t = 0.125 \cdot ns$ ($\Delta s = 1.5 \cdot inches$) up to 1.125 ns or 15 inches. The images are displayed in order of increasing time from left to right and top to bottom with the image in the lower right corner of Figure 4.20 corresponding to $t_0 = 1.125 ns$. Note that in the final image, the fields have decayed more than 25 dB from the peak scattering level at $t_0 = 0 \cdot ns$. As expected, with each incremental shift, the fields appear to spread outward in a radial direction from the origin corresponding to later time. The concentric rings increase in diameter as time increases representative of the scattered fields propagating away from the sphere.

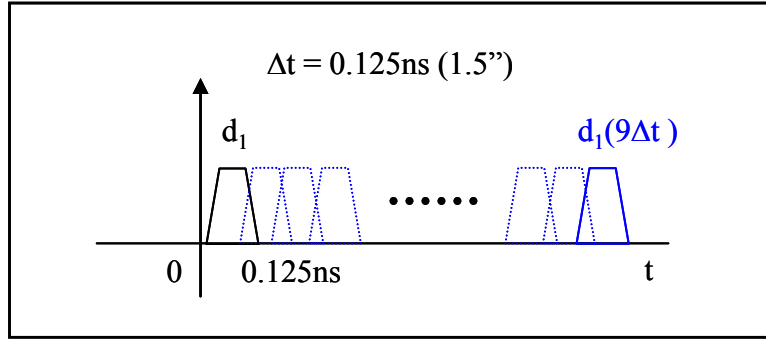


Figure 4.19 Time Domain Representation of Sliding Gate

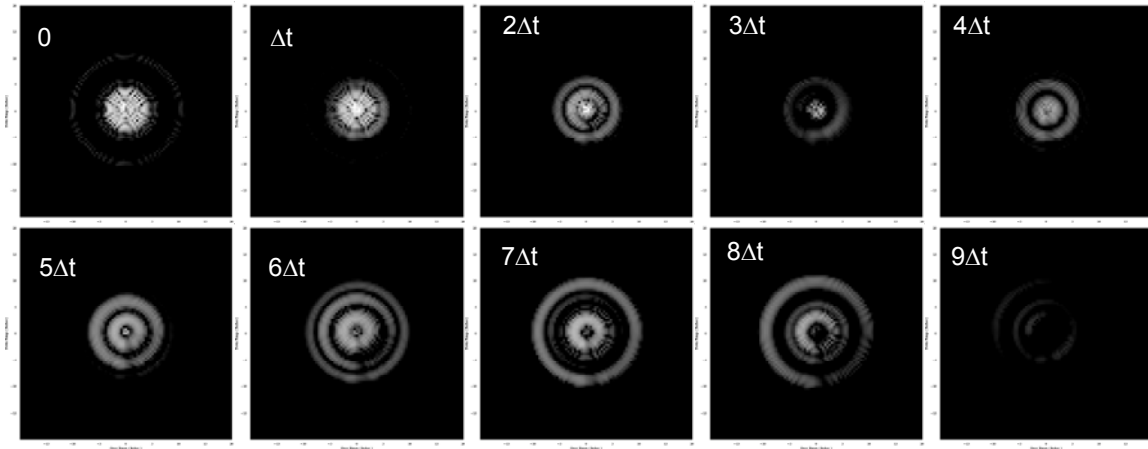


Figure 4.20 ISAR Images Metal Sphere d_1 with progressive shifts $t_0 = 0$ to $9\Delta t$, $\Delta t = 0.125ns$

These results indicate that wavelet analysis in combination with a sliding time gate may be used to further analyze scattering phenomena in radar images.

4.3.2 Gated Scattering Response Metal Triangle

The images in Figure 4.21 represent the scattering response of the triangular target after sliding the gate 0.5 ns or six inches. Comparison of Figure 4.21(a) with Figure 4.10(a) reveals that diffraction from the ends of the rods, as opposed to the specular scattering, is now visible in the image corresponding to a_1 . By sliding the gate, scattering sources, which are six inches from the reference, are now selected by

the lower resolutions. The initial ISAR image in Figure 4.10(a) results from a time gate centered at $t = 0 \cdot ns$ with a width of 0.125 ns. By sliding the signal 0.5 ns earlier in time, the later time response due to the diffraction from the tips of the rods is now contained in the gate corresponding to a_1 . Similarly, as resolution increases, the later time scattering phenomena are selected, relative to 0.5 ns. The initial specular scattering response visible in Figure 4.10(a) does not appear in the images. In the image corresponding to d_2 , Figure 4.21(c), the fields in the region of the specular response, appear to be spreading outward in a direction normal to each of the rods. Once again, as the resolutions increase, the fields begin to decay, approaching zero by the image corresponding to d_5 , Figure 4.21(f)

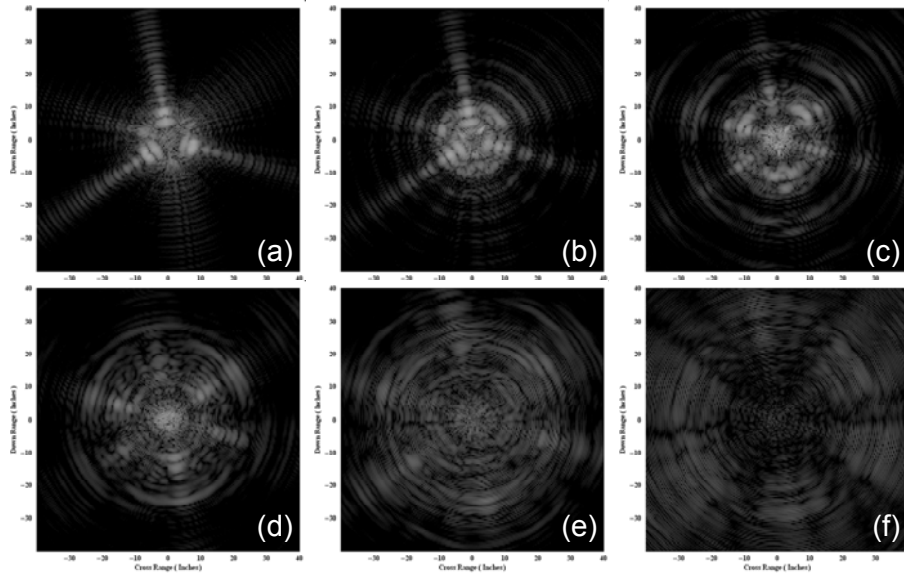


Figure 4.21 Multi-Resolution ISAR Images Triangular Target ($t_0 = 0.5ns$) (a) Approximation 1 and (b-f) Details 1-5

Through comparison of the original images (Figure 4.10) to the shifted images (Figure 4.21), it is apparent that the fields decay earlier. The overall levels in Figure 4.21 (d), (e) and (f) are lower than the corresponding images in Figure 4.10. This further confirms that the applied phase shift to the spectral domain scattered field combined with the wavelet analysis is a means to extract scattering phenomena at different instances in time. As with the case of the metal sphere, progressive phase shifts are applied to a single resolution of the scattered field to further observe wave medium interaction phenomena.

Figure 4.22 contains the time domain representation of the sliding gate implemented for test case 2. Again d_1 is utilized in the analysis. The gate is shifted from 0 to $19\Delta t$, where $\Delta t = 0.125$ ns. The resulting images for progressive phase shifts are shown in Figure 4.23. As before, the images are normalized to the peak scattering level obtained for the sphere by itself for a 0.125 ns wide gate centered at $t = 0 \cdot ns$. The first image (upper left corner) corresponds to the initial image at $t_0 = 0 \cdot ns$. Progressive phase shifts are applied with successive time increments for $\Delta t = 0.125$ ns ($\Delta s = 1.5''$). The series of images starts at $t_0 = 0 \cdot ns$ and progresses to 2.375 ns or 28.5 inches, for the image in the lower right corner of Figure 4.23. Initially, the specular scattering appears and is the only response visible for $t_0 = 0 \cdot ns$ to 0.375 ns. As the gate slides later in time, the diffraction from the corners of the triangle becomes visible for $t_0 = 0.5 \cdot ns$ and increases in amplitude for several time steps. As time progresses the specular scattering diminishes completely by $t_0 = 1.625 \cdot ns$. The scattering

phenomena due to the triangle corners decay as well until, in the final image, the fields are more than 25 dB below the peak scattering response.

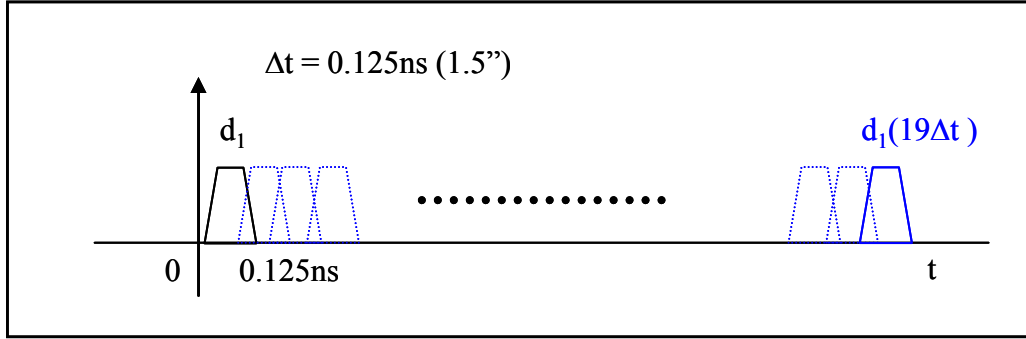


Figure 4.22 Time Domain Representation of Sliding Gate

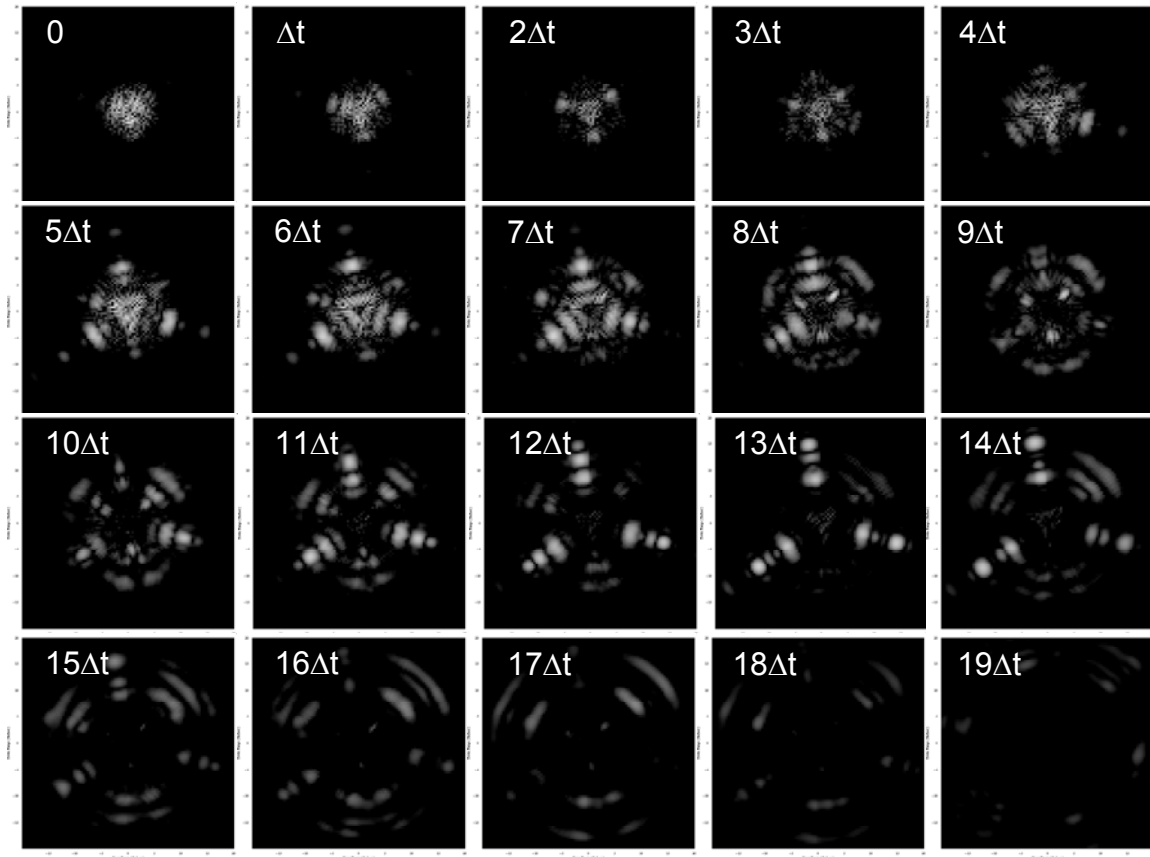


Figure 4.23 ISAR Images Metal Triangular Target d_1 with progressive shifts $t_0 = 0$ to $19\Delta t$, $\Delta t = 0.125\text{ns}$

4.3.3 Gated Scattering Response Multiple Targets

Next, a sliding time gate is implemented for test case 3 consisting of the metal sphere and the triangular target with a seven inch separation. Initially the time gate is shifted by setting $t_0 = 0.5 \cdot ns$. Multi-resolution images generated for the lowest six resolutions are shown in Figure 4.24. The images indicate that the scattering from the sphere is still contained in the lower resolutions, Figure 4.24 (a) and (b), as in the original images (Figure 4.13(a) and (b)). Similarly, the scattering response from the triangle becomes evident in the image corresponding to d_2 , Figure 4.24 (c). In Figure 4.24 (d) and (e) the shape of the triangle is still visible as the fields spread outward. As before, the fields tend towards zero for the highest resolution Figure 4.24 (f)

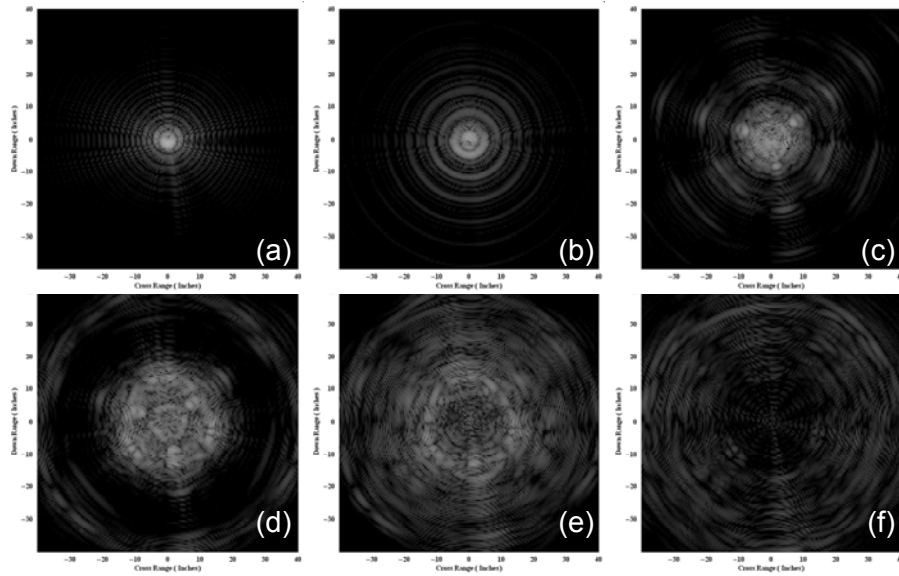


Figure 4.24 Multi-Resolution ISAR Images Metal Sphere & Triangle $dz = 7''$
($t_0 = 0.5ns$) (a) Approximation 1 and (b-f) Details 1-5

Since the changes were insignificant, a larger phase shift, corresponding to a time shift of 1.25 ns, was applied to the scattered field. The images for the lowest six

wavelet resolutions were generated and shown in Figure 4.25. The image corresponding to a_1 in Figure 4.25 (a) is representative of the scattering phenomena of the triangular target. These results are comparable to the lowest approximation in Figure 4.10 (a), for test case 2 with the triangle by itself. Other scattering phenomena is visible in this case due to the addition of coupling to the sphere. The first two resolutions, Figure 4.25(a) and (b) are representative of the specular scattering response seen previously in the images for the triangle only. The diffraction of the fields can be seen where the metal rods meet in Figure 4.25 (d) and (e). The scattering response from the sphere is not specifically visible except for the added interactions that appear as circular rings in all of the images.

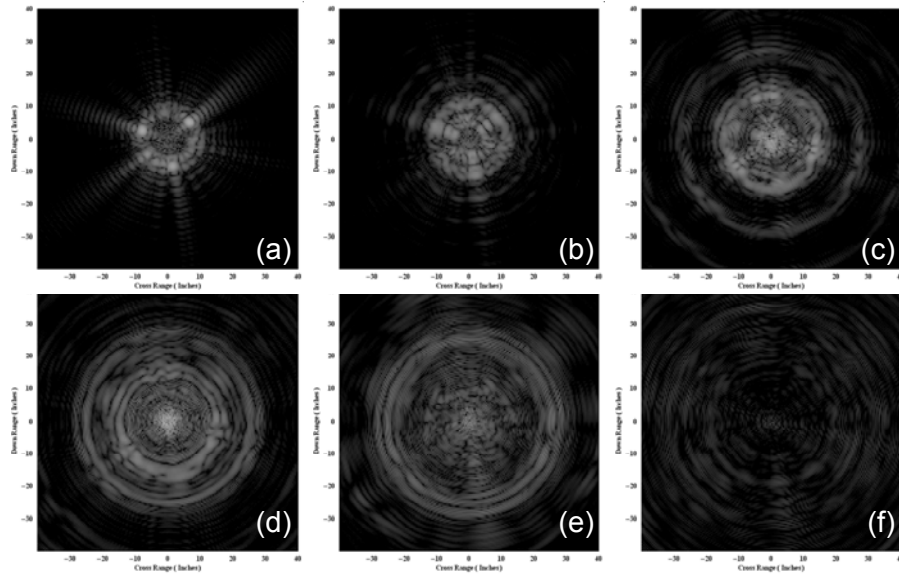


Figure 4.25 Multi-Resolution ISAR Images Metal Sphere & Triangle $dz = 7''$
 $(t_0 = 1.25ns)$ (a) Approximation 1 and (b-f) Details 1-5

The final test case, consisting of the sphere and triangle configured with a separation of eleven inches, was processed in the same manner as test case 3 for

comparison purposes. The ISAR images shown in Figure 4.26 consist of the lower six resolutions with the gate centered at $t = 0.5 \cdot ns$. Comparison of these images to the initial images (Figure 4.16) shows a slight change in the response. The response from the sphere still appears in the lower three resolutions, Figure 4.26 (a-c), and the scattering from the triangle becomes visible in the higher resolutions, Figure 4.26 (d-f). The most significant variations appear in the lower resolutions where the spreading becomes more significant in Figure 4.26 (a-b) than in Figure 4.16 (a-b) and the initial indications of coupling with the triangle is visible in Figure 4.26 (c) while it is not visible in Figure 4.16 (c).

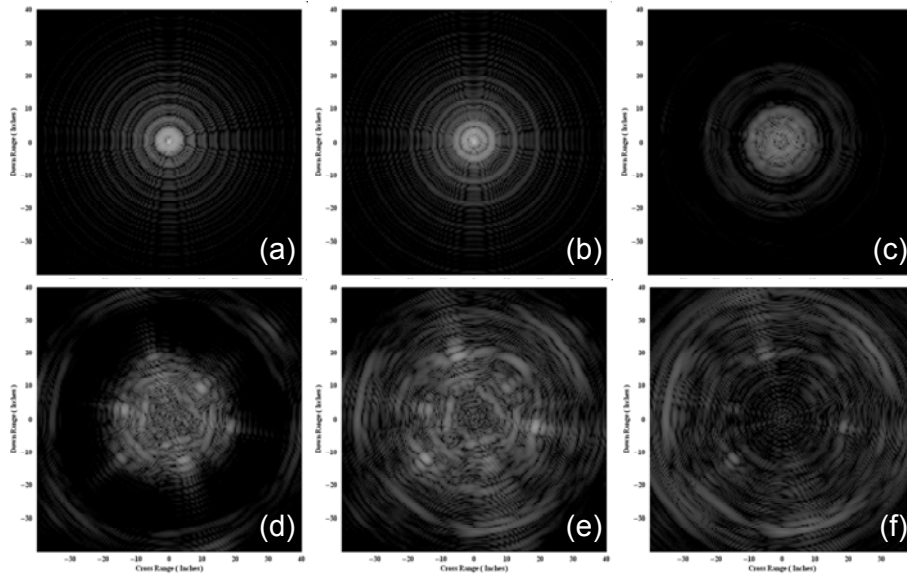


Figure 4.26 Multi-Resolution ISAR Images Metal Sphere & Triangle $dz = 11''$
 $(t_0 = 0.5 \cdot ns)$ (a) Approximation 1 and (b-f) Details 1-5

To evaluate the response of sliding the gate, further from the reference, images were created with the gate centered at $t = 1.25 \cdot ns$, Figure 4.27. Significant differences appear between the images in Figure 4.26 and Figure 4.27. The strong specular

scattering from the sphere that was apparent in the lower resolutions of Figure 4.26 (a-c) is no longer visible in Figure 4.27 (a-c). The specular scattering from the cylindrical rods appears in the image corresponding to d_1 , Figure 4.27 (b) instead of d_3 , Figure 4.26 (d).

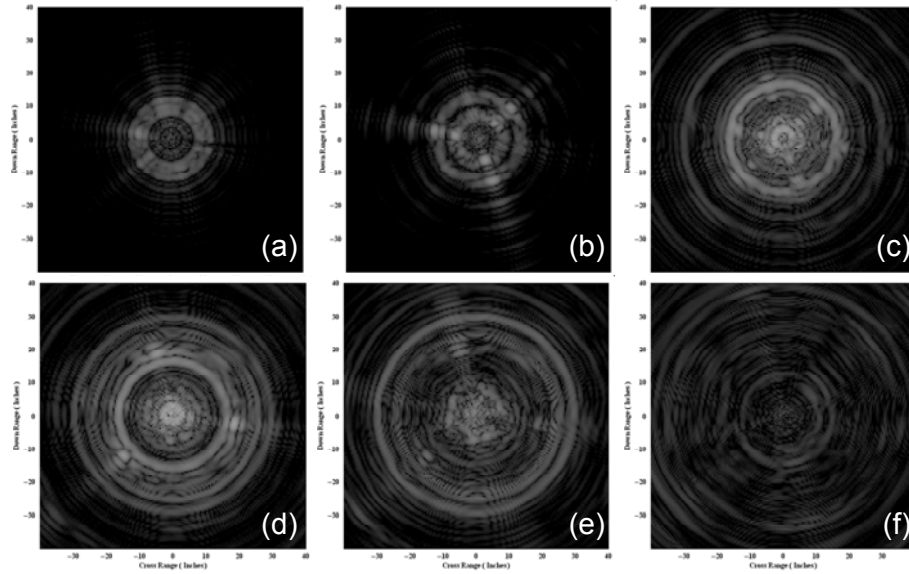


Figure 4.27 Multi-Resolution ISAR Images Metal Sphere & Triangle $dz = 11''$
($t_0 = 1.25ns$) (a) Approximation 1 and (b-f) Details 1-5

In the final step, progressive phase shifts were applied to the fields corresponding to d_1 . The time domain representation of the 0.125 ns sliding gate is depicted in Figure 4.28. The series of images created from incrementally sliding the gate are shown in Figure 4.29. These images are also normalized to the peak value of the sphere by itself. The first image (upper left corner) begins with a 0.125 ns gate centered at $t = 0 \cdot ns$. The gate is moved incrementally ($\Delta t = 0.125$ ns, $\Delta s = 1.5''$) to 2.375 ns or 28.5 inches. The image in the lower right corner of Figure 4.29 is for a gate

centered at 2.375 ns. The scattering response from the sphere is evident from $t_0 = 0$ to $t_0 = 1 \cdot ns$ and the response is nearly identical to the response for test case 1, Figure 4.20 of the sphere by itself. The scattering response from the triangle first becomes visible for $t_0 = 1.25 \cdot ns$. As in test case 2, the specular scattering is visible prior to the diffraction from the ends of the rods. As expected, with each incremental shift, the fields appear to spread in a radial direction from the origin corresponding to selectively gating later time scattering responses.

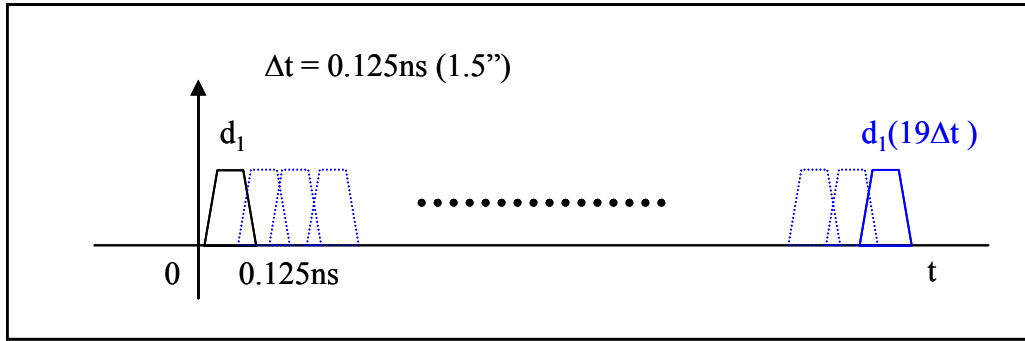


Figure 4.28 Time Domain Representation of Sliding Gate

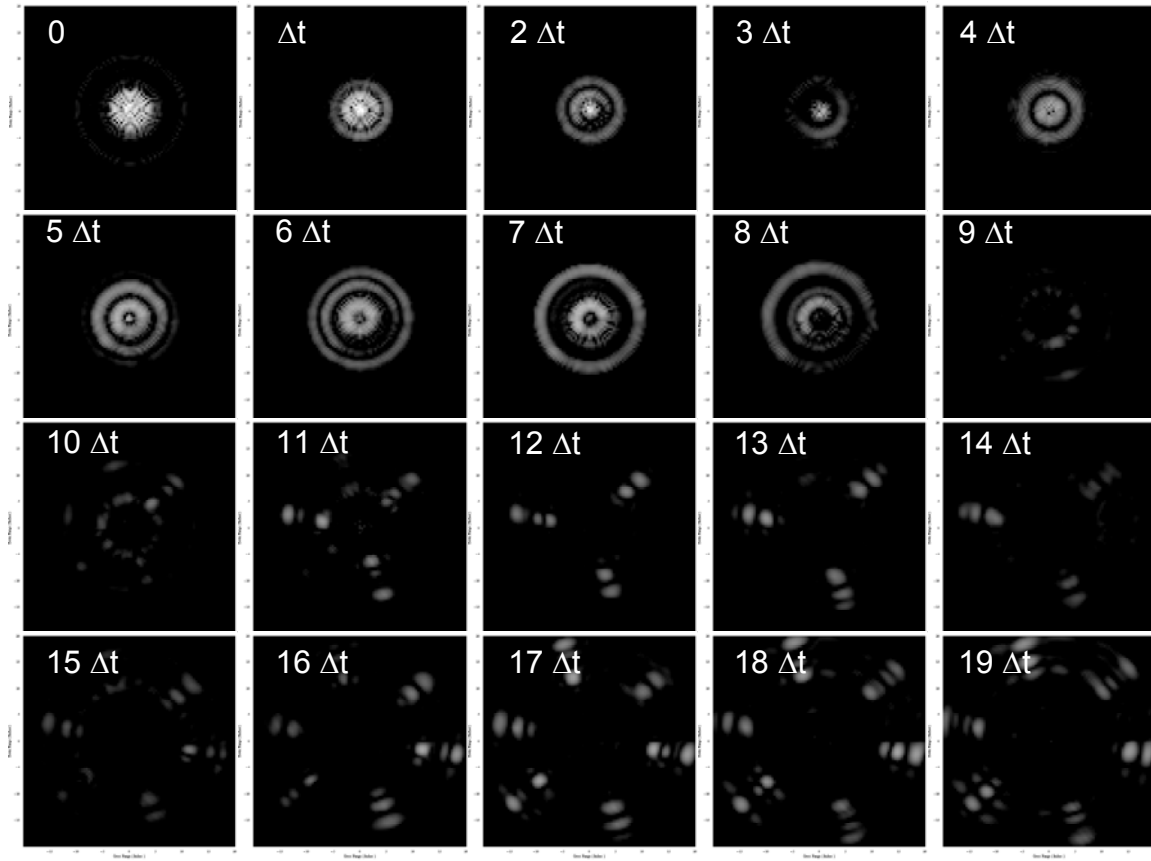


Figure 4.29 ISAR Images Sphere and Triangle ($dz = 11''$) d_1 with progressive shifts $t_0 = 0$ to $19\Delta t$, $\Delta t = 0.125ns$

The results presented in this section indicate that the generation of ISAR images from multi-resolution frequency domain data allows for visualization and separation of scattering phenomena. Additionally, it has been shown that a sliding time (range) gate, implemented with wavelet analysis, provides an efficient means to further analyze wave medium interaction phenomena.

CHAPTER 5

CONCLUSIONS

The findings presented in this thesis are a continuation of the work contained in [2] where it was determined that multi-resolution analysis could be used for clutter rejection through selection of resolutions corresponding to scattering phenomena occurring at earlier or later arrival times. This thesis was initiated to further investigate the use of multi-resolution frequency domain analysis for examination of scattering phenomena in radar images through implementation of a sliding range gate. The initial hypothesis stated that a sliding range gate could be implemented by combining a frequency domain phase shift with multi-resolution analysis for extraction of scattering phenomena at specific instances in time. Selective positioning of the range gate provides a means to fully analyze the data through separation of scattering centers and visualization of the evolution of the scattered fields in time.

Scattering measurements were performed for several test configurations, as described in Chapter 3, in order to experimentally demonstrate the use of multi-resolution frequency domain analysis to separate wave medium interaction phenomena from metallic targets in radar images. Quasi-monostatic radar cross section measurements were made of a four inch diameter metal sphere and of three open ended metal rods formed in a triangular configuration. After measuring the objects separately, the sphere and the triangle were measured together with the sphere positioned on a foam

column above the triangle centered on the axis of rotation. This configuration was repeated with the sphere located at two different heights to demonstrate that the relative separation between the two targets could be detected. Standard ISAR imaging techniques were used to evaluate the multi-resolution results for each test case.

The results presented in Chapter 4, indicate that the scattering phenomena from multiple targets can be separated using wavelet analysis. It was shown that a sliding range gate could be implemented and utilized to detect relative separations between two known targets. Initially, the targets were characterized independently to examine the scattering phenomena in the corresponding ISAR images. Multi-resolution images were created to examine changes in the fields with respect to time. Phase shifts were applied to the frequency domain data and the resulting images indicated that the scattering phenomena from later times could be shifted to earlier time for extraction with lower resolutions.

These measurement and processing steps were repeated for two test cases containing the metal sphere and triangle target. Analysis of the multi-resolution images validated that the relative separation between the two targets could be detected. For the final processing step, d_1 , corresponding to a 0.125 ns wide gate, was selected and incremental phase shifts were applied to generate a series of images. These images reveal the progression of the fields with respect to time. For the final test case (sphere and triangle with 11" separation), the 0.125 ns wide gate was moved from 0 to 2.375 ns in 0.125 ns steps. The images shown in Figure 4.29 correspond to each time step and demonstrate that selective positioning of the gate allows for separation of scattering

sources. The images from time steps 0 ns through 1.125 ns closely match those of the sphere by itself, Figure 4.20, while the images from 1.25 ns to 2.375 ns correspond to the scattering phenomena from the triangle.

It has been shown experimentally that wavelet analysis provides a means to reduce clutter as well as detect targets. It was also demonstrated that the lower resolutions obtained from the wavelet decomposition correspond to earlier arrival times and that the higher resolutions correspond to later arrival times, relative to the reference position. Furthermore, these results support the hypothesis that the application of the wavelet transform, to phase shifted frequency domain data, is a means to implement a sliding range gate. Finally, an efficient means to remove window effects was implemented through removal of the lowest approximation prior to reconstruction of the signal.

The wavelet analysis performed was limited to the Daub2 wavelet. Further studies should include evaluations of other wavelets to determine if the properties specific to individual wavelets correlate to various scattering phenomena. For this study, the length of the wavelet was selected such that relatively small changes over time could be observed. Since the temporal increment is determined by the frequency bandwidth, future work should include measurements covering a broader frequency band. By increasing the time domain resolution, a higher order filter could be utilized to maximize clutter rejection while maintaining the selectivity of the gate in the spatial domain.

This study was also limited to a single polarization for transmit and receive of the incident and scattered fields. Future studies utilizing fully polarimetric scattering data may prove interesting due to the polarization dependent scattering characteristics of objects. Additional work may also include bistatic measurements since the experimental test cases presented were only for a quasi-monostatic configuration. Multi-resolution analysis applied to bistatic measurements may provide further insight into the extraction of wave medium interaction phenomena in radar images.

Finally, the developed methodology should be applied to complex targets and targets embedded in medium. Only metallic targets were considered in this study therefore examination of other types of targets would prove useful and provide practical application.

APPENDIX A

MATHEMATICA MULTI-RESOLUTION PROGRAM

```

(***** MAIN PROGRAM *****)
This program reads in UTA range data after calibration and background subtraction have been applied. The
data has already been interpolated to a power of two to maximize the number of resolutions obtained with
the multiresolution analysis. A data file for each azimuth angle (72 angles) containing 1024 frequency
points is read and processed. This program processes the data files at each azimuth angle and exports
processed data after each step allowing for review of intermediate results. Window effects are removed
via application of wavelet analysis. Phase shift is applied. Individual resolutions are obtained through
wavelet analysis. Conjugate phase shift is applied. Finally resulting data files for all azimuth angle
are concatenated and exported to a single file which is read by polar reformatting routine prior to ISAR images are created.
*****
(***** File Structure *****)
The following directory structure should be created prior to running the program.

(*datapth/interp - contains interpolated, calibrated data*)
(*datapth/rmwve - for files with window effects removed*)
(*datapth/phshft - for files with phase shift applied*)
(*datapth/wt - for files after wavelet decomposition & reconstruction*)
(*datapth/rmwphshft - for files with phase shift removed*)
*****
(***** Notes *****)
(*1. Window Effects - Hard wired for 1024 points, maximum decompositions nine in this case, and 2nd order filter.*)
(*2. Limited to reconstruction of sequential resolutions. ie If detail is set to six,
resolutions one thru six will be reconstructed.*)
(*3. Limited to Daubechies filter. *)
(*4. No error checking is included to prevent exceeding maximum number of decompositions which is determined
by number of data points, filter length.*)

*****
<< LinearAlgebra`MatrixManipulation`
<< Wavelets`Wavelets`
<< Miscellaneous`PhysicalConstants`
c = SpeedOfLight (Second/Meter) / 10^9 // N;

(***** CONCATENATE FILES MODULE *****)
(* Concatenates data for each azimuth angle and writes complex data to file. Zero degree azimuth file is used for az=
0 and az=360 *)

ConcatenateFiles[inpth_, outpth_, fname_, nfreq_, naz_, data_, expt_] :=
Module[{n, dataout},
data = Table[0, {nfreq}, {naz + 1}];
data[[All, 1]] = ReadList[StringJoin[inpth, fname, ToString[naz - 1]], Complex[Real, Real]];
Do[data[[All, n + 1]] = ReadList[StringJoin[inpth, fname, ToString[n - 1]], Complex[Real, Real]], {n, naz}];
dataout = Flatten[data];
If[expt == 1, Export[StringJoin[outpth, fname], Transpose[{Re[dataout], Im[dataout]}], "Table"]];
ClearAll[n];
];

(***** WAVELET TRANSFORM MODULE *****)
(* Applies wavelet transform and inverse transform frequency data for a single azimuth angle. Limited to Daubechies filter,
with periodic boundary conditions. Real and imaginary parts are decomposed and reconstructed independently. The
number of decompositions is set with decomp and coefficients for reconstruction is set with selcfft. Note
that all coefficients other than selcfft are set to zero prior to inverse wavelet transform. *)

```

```

WDData[nfreq_, pth_, wtdataoutpth_, fname_, ind_, detail_, selcfff_, order_, decomp_] :=
Module[{data, h, wtrealdata, wtinagdata, realdetail, inagdetail, cmplxdetail},

data = Take[ReadList[StringJoin[pth, fname, ind], Complex[Real, Real]], nfreq];
h = DaubechiesFilter[order];

wtrealdata = WaveletTransform[Re[data], h, decomp, BoundaryCondition -> Periodic];
wtinagdata = WaveletTransform[Im[data], h, decomp, BoundaryCondition -> Periodic];

realdetail = InverseWaveletTransform[wtrealdata - MapAt[# - # &, wtrealdata, selcfff], h, BoundaryCondition -> Periodic];
inagdetail = InverseWaveletTransform[wtinagdata - MapAt[# - # &, wtinagdata, selcfff], h, BoundaryCondition -> Periodic];
cmplxdetail = realdetail + I inagdetail;

Export[StringJoin[wtdataoutpth, fname, ToString[decomp], "dcmpd", ToString[order], "wtd", ToString[detail], ind],
Transpose[{Re[cmplxdetail], Im[cmplxdetail]}], "Table"];
Clear[cmplxdetail, realdetail, inagdetail, wtrealdata, wtinagdata, h];
];

(***** PHASE SHIFT MODULE *****)
(* Phase shift is applied to complex data for a single azimuth angle. *)

PhaseShiftData[n_, nfreq_, df_, fmin_, naz_, intdataoutpth_, shftdataoutpth_, fname_, ind_] :=
Module[{data, datashft, freq},

freq = df * (Range[nfreq] - 1) + fmin;
t0 = 1 / (2. nfreq df) // N;
timeshft = n t0;
phsft[f_] := Exp[-I f 2. Pi (timeshft)];

data = ReadList[StringJoin[intdataoutpth, fname, ind], Complex[Real, Real]];
datashft = data (phsft[freq]);

Export[StringJoin[shftdataoutpth, fname, "pshft", ToString[n], ind], Transpose[{Re[datashft], Im[datashft]}], "Table"];
ClearAll[datashft, data];
];

(***** INPUT PARAMETERS *****)
PTH - WORKING DIRECTORY
DATAPTH - DIRECTORY CONTAINING DATA (MEASURED & PROCESSED)
INPTH - DIRECTORY TO "READ" DATA FROM
OUTPTH - DIRECTORY TO "WRITE" DATA TO
INFN - ROOT FILENAME OF INPUT DATA
NFREQ - NUMBER OF FREQUENCIES
NAZ - NUMBER OF AZIMUTH ANGLES
FMIN - LOWER FREQUENCY LIMIT
FMAX - UPPER FREQUENCY LIMIT
TIMESHFT - APPLIED TIME SHIFT
DETAIL - NUMBER OF RESOLUTIONS TO RECONSTRUCT
ORDER - FILTER ORDER
DECOMP - NUMBER OF DECOMPOSITIONS

*****)

pth = "C:\\Documents and Settings\\Nancy\\My Documents\\Datanew\\";
datapth = StringJoin[pth, "spheretri2\\"];
inpth = StringJoin[datapth, "interp\\"];
outpth = StringJoin[datapth, "rmvve\\"];
infn = "trispclrbfsint";

nfreq = 1024.;
naz = 72.;
fmin = 4; (*GHz*)
fmax = 8; (*GHz*)
timeshft = -0.5; (*ns*)
detail = 6;
order = 2;
decomp = 9;

```


APPENDIX B

MATHEMATICA CALIBRATION PROGRAM

```

(*****)

ConcatenateFiles[inpth_, outpth_, fname_, nfreq_, naz_, data_, expt_] :=
Module[{n, dataout},
  data = Table[0, {nfreq}, {naz + 1}];
  data[[All, 1]] = ReadList[StringJoin[inpth, fname, ToString[naz - 1]], Complex[Real, Real]];
  Do[data[[All, n + 1]] = ReadList[StringJoin[inpth, fname, ToString[n - 1]], Complex[Real, Real]], {n, naz}];
  dataout = Flatten[data];
  If[expt == 1, Export[StringJoin[outpth, fname], Transpose[{Re[dataout], Im[dataout]}], "Table"]];
  ClearAll[n];
];

(*****)

CalibrateData[pth_, caldataoutpth_, fnbkg_, pthbkg_, fntrgt_, pthtrgt_, caldata_, bkgcaldata_, thdata_, ind_] :=
Module[{outpth, bkgdata, trgtdata, trgtdatacal},
  bkgdata = ReadList[StringJoin[pth, pthbkg, fnbkg, ToString[ind]], Complex[Real, Real]];
  trgtdata = ReadList[StringJoin[pth, pthtrgt, fntrgt, ToString[ind]], Complex[Real, Real]];
  trgtdatacal = thdata + (trgtdata - bkgdata) / (caldata - bkgcaldata);

  Export[StringJoin[caldataoutpth, fntrgt, "cal", ToString[ind]], Transpose[{Re[trgtdatacal], Im[trgtdatacal]}], "Table"];
  ClearAll[bkgdata, trgtdata, trgtdatacal];
];

(*****)

(*****INPUT PARAMETERS*****
PTH - WORKING DIRECTORY
DATAPTH - DIRECTORY CONTAINING MEASURED DATA FILES, CALIBRATION, BACKGROUND, AND PROCESSED DATA
PTHBKG - DIRECTORY CONTAINING MEASURED BACKGROUND
PTHTRGT - DIRECTORY CONTAINING MEASURED TARGET
FNBKG - BACKGROUND ROOT FILENAME (ie "tribac" - tribac0, tribac1, ... .. tribac72)
FNTRGT - TARGET ROOT FILENAME (ie "trisp" - trisp0, trisp1, ... .. trisp72)
CALFILE - MEASURED CALIBRATION SPHERE AT AZ EQUAL ZERO
BKGCALE - BACKGROUND AT AZ EQUAL ZERO
THFILE - THEORETICAL SCATTERING CALIBRATION STANDARD (IN THIS CASE: 4 INCH SPHERE)
NFREQ - NUMBER OF FREQUENCIES
NAZ - NUMBER OF AZIMUTH ANGLES
FMIN - LOWER FREQUENCY LIMIT
FMAX - UPPER FREQUENCY LIMIT
*****)

pth = "C:\\Documents and Settings\\Nancy\\My Documents\\DataNew\\";
datapth = StringJoin[pth, "spherecyl\\"];
pthbkg = "tarbac\\";
pthtrgt = "sphcyl\\";
fnbkg = "tarbac";
fntrgt = "cylsp6";

calfile = StringJoin[datapth, "calsph\\calsp60"];
bkgcalfile = StringJoin[datapth, "bkgnd\\calbac0"];

thfile = StringJoin[pth, "Theoretical\\6inspheretheor.dat"];

nfreq = 801.;
naz = 72.;
fmin = 4;
fmax = 8;

```

```

(*****PARAMETERS*****)

CALDATA - COMPLEX LIST CONTAINING MEASURED CALIBRATION STANDARD AT AZ EQUAL ZERO
BKGCALDATA - COMPLEX LIST CONTAINING MEASURED BACKGROUND AT AZ EQUAL ZERO
THDATA - COMPLEX LIST CONTAINING THEORETICAL SCATTERING FROM CAL STANDARD
CALDATAPATH - OUTPUT PATH FOR CALIBRATED DATA
FNCAL - CALIBRATED TARGET ROOT FILENAME (ie "trispal" - trispal0, trispal1, .... trispal72)
*****)

(*****READ DATA*****)
caldata = ReadList[ calfile, Complex[Real, Real] ];
bkgcalddata = ReadList[ bkgcalfile, Complex[Real, Real] ];
thdata = ReadList[ thfile, {Real, Complex[Real, Real]} ];
thdata = thdata[ [ All, 2 ] ];
*****)

caldatapath = StringJoin[ datapath, "cal\\" ];

Do[CalibrateData[ datapath, caldatapath, fnbkg, pthbkg, fntgrt, pthtrgt, caldata, bkgcalddata, thdata, n - 1], {n, naz}];
Clear[ caldata, bkgcalddata, thdata ];
fncal = StringJoin[ fntgrt, "cal" ];

Clear[data2d]
ConcatenateFiles[caldatapath, datapath, fncal, nfreq, naz, data2d, 1];

```

APPENDIX C

MATHEMATICA POLAR FORMAT PROGRAM

```

<< Miscellaneous`PhysicalConstants`
<< LinearAlgebra`MatrixManipulation`
$HistoryLength = 0;
c = SpeedOfLight (Second / Meter) / 10^9 // N;
dtr = Pi / 180.;

CreateKspaceData[n_, dk_, data_, kmn_, kmx_, azmn_, azmx_, kspdata_] :=
Module[{m, pyarr, pxarr, redatainterp, indatainterp, pkarr2d, ptharr2d},

  m = 2 n;
  pyarr = {dk * (-Range[m]) + n * dk};
  pxarr = {dk * (Range[m]) - n * dk};

  finterpre = ListInterpolation[Re[data], {{kmn, kmx}, {azmn, azmx}}];
  finterpim = ListInterpolation[Im[data], {{kmn, kmx}, {azmn, azmx}}];

  pkarr2d = Table[Sqrt[pxarr[[i]]^2 + pyarr[[j]]^2], {i, m}, {j, m}];
  ptharr2d = Table[0, {m}, {m}];

  Do[If[(pxarr[[i]] == 0) && (pyarr[[j]] == 0), ptharr2d[[i, j]] = 0,
    ptharr2d[[i, j]] = If[ArcTan[pxarr[[i]], pyarr[[j]]] * 180. / Pi < 0, 360 + ArcTan[pxarr[[i]], pyarr[[j]]] * 180. / Pi,
      ArcTan[pxarr[[i]], pyarr[[j]]] * 180. / Pi], {i, m}, {j, m}];

  reinterpdata = Table[0, {m}, {m}];
  Do[reinterpdata[[i, j]] = If[(kmn ≤ pkarr2d[[i, j]] ≤ kmx) && (azmn ≤ ptharr2d[[i, j]] ≤ azmx),
    finterpre[pkarr2d[[i, j]], ptharr2d[[i, j]], 0], {i, m}, {j, m}];
  iminterpdata = Table[0, {m}, {m}];

  Do[iminterpdata[[i, j]] = If[(kmn ≤ pkarr2d[[i, j]] ≤ kmx) && (azmn ≤ ptharr2d[[i, j]] ≤ azmx),
    finterpim[pkarr2d[[i, j]], ptharr2d[[i, j]], 0], {i, m}, {j, m}];

  kspdata = reinterpdata + I iminterpdata;
];

(*****INPUT PARAMETERS*****
  PTH - WORKING DIRECTORY
  INFN - ROOT FILENAME OF INPUT DATA
  NFREQ - NUMBER OF FREQUENCIES
  FMN - LOWER FREQUENCY LIMIT
  FMX - UPPER FREQUENCY LIMIT
  AZMN - LOWER AZIMUTH LIMIT
  AZMX - UPPER AZIMUTH LIMIT
  DAZ - AZIMUTH INCREMENT
  TH - THETA ANGLE
  ND - NUMBER OF DECOMPOSITIONS

  NAZ - NUMBER OF AZIMUTH ANGLES
  *****)

```

```

pth = "C:\\Documents and Settings\\Nancy\\My Documents\\Datanew\\";
datapth = StringJoin[pth, "spheretri2\\" ]
m = -4;
infn = StringJoin["trispcalintpshft", ToString[m], "9dcmpd2wtd"];

nfreq = 1024;
fnn = 4;
fmn = 8;

azmn = 0;
azmx = 360;
daz = 5;

theta = 60.;

dk = 0.5;

nd = 6;
(*****)

naz = (azmx - azmn) / daz + 1;

kmn = (2 Pi fnn / c) Sin[theta Pi / 180.];
kmx = (2 Pi fmn / c) Sin[theta Pi / 180.];

numpts = Floor[kmx / dk] + 1;

(*****)

Do[
  fname = StringJoin[infn, ToString[dt], "pshft", ToString[-m]];
  (*fname =StringJoin["trispcalinttgr19dcmpd2wtd", ToString[dt]];*)
  data = Partition[ReadList[StringJoin[datapth, fname], Complex[Real, Real]], naz];
  Clear[kspdata];
  CreateKspaceData[numpts, dk, data, kmn, kmx, azmn, azmx, kspdata];
  dataout = Flatten[kspdata];
  outfame = StringJoin[fname, "pdk1"];

  Export[StringJoin[datapth, outfame], Transpose[{Re[dataout], Im[dataout]}], "Table"];, {dt, nd}];

```

APPENDIX D

MATHEMATICA ISAR PROGRAM

```

<<LinearAlgebra`MatrixManipulation`

SetOptions[ListDensityPlot,
    Mesh→False,
    TextStyle→{FontSize→14, FontFamily→"Times", FontWeight→"Bold"}];

(*****)

CreateImage[data2d_, n_, dk_, imag_, r_, h_] :=
Module[{r0, half, npts, tempimage, sub1, sub2, sub3, sub4},
    half = Floor[n/2];
    h = half[[1]];
    npts = Length[Flatten[data2d]] - Length[Select[Abs[Flatten[data2d]], # == 0.0 &]];
    tempimage = InverseFourier[data2d, FourierParameters→{-1, 1}]/(npts);
    sub1 = SubMatrix[tempimage, {1, 1}, {h, h}];
    sub2 = SubMatrix[tempimage, {h, 1}, {h, h}];
    sub3 = SubMatrix[tempimage, {h, h}, {half[[1]], h}];
    sub4 = SubMatrix[tempimage, {1, h}, {half[[1]], h}];
    imag = Transpose[Join[Transpose[Join[sub3, sub4]], Transpose[Join[sub2, sub1]]]];
    r0 = (Pi)/(n dk)/0.0254;
    r = Range[-nr0/2, (n-1)r0/2, r0];
];

(*****)

pth = "C:\\Documents and Settings\\Nancy\\My Documents\\DataNew\\";
datapth = StringJoin[pth, "spheretri2\\" ];
fname = "trispalintpsht-49dcmpd2wtd3psht4pdk1";
data = ReadList[StringJoin[datapth, fname], Complex[Real, Real]];
dk = 0.5;
numpts = Sqrt[Dimensions[data]];
data2d = Partition[data, numpts];

CreateImage[data2d, numpts, dk, isarimage, rng, half];

(*****)

ListDensityPlot[20 Log[10, Abs[data2d + 10^-20]], Mesh→False, MeshRange→{{-189, 189}, {-189, 189}},
    PlotRange→{-25, -15}, FrameLabel→{"Kx", "Ky"}]

ListDensityPlot[20 Log[10, Abs[isarimage]], PlotRange→{{-20, 20}, {-20, 20}, {-80, -35}},
    MeshRange→{{Min[rng], Max[rng]}, {Min[rng], Max[rng]}}, FrameLabel→{"Cross Range ( Inches )", "Down Range ( Inches )"}]

ListPlot[Transpose[{rng[[1, All]], 20 Log[10, Abs[isarimage][[half, All]] ]}], PlotJoined→True,
    PlotRange→{{-40, 40}, {-90, -20}}, Frame→True, FrameLabel→{"Cross Range (Inches)", "Scattering (dBsm)"},
    PlotStyle→{Thickness[.005]}, GridLines→Automatic];

ListPlot[Transpose[{rng[[1, All]], 20 Log[10, Abs[isarimage][[All, half]] ]}], PlotJoined→True,
    PlotRange→{{-20, 20}, {-80, -30}}, Frame→True, FrameLabel→{"Down Range (Inches)", "Scattering (dBsm)"},
    PlotStyle→{Thickness[.005]}, GridLines→Automatic];

ListDensityPlot[20 Log[10, Abs[isarimage]/Max[Abs[isarimage]]], PlotRange→{{-20, 20}, {-20, 20}, {-45, 0}},
    MeshRange→{{Min[rng], Max[rng]}, {Min[rng], Max[rng]}}, FrameLabel→{"Cross Range ( Inches )", "Down Range ( Inches )"}];

Quit

```


APPENDIX E

MATHEMATICA PROGRAM SPHERE THEORETICAL SCATTERING

```

<< Miscellaneous`PhysicalConstants`
c = SpeedOfLight (Second / Meter) / 10^9 // N
0.299792

freq = (16 / 1023) (Range[1024] - 1) + 2 // N;

landa = c / freq // N;

k = 2 Pi / landa // N;

radius = 2 * 0.0254

0.0508

ka = k * radius;

SphericalBesselJ[n_, z_] := Sqrt[Pi / (2. z)] BesselJ[n + 0.5, z]
SphericalBesselY[n_, z_] := Sqrt[Pi / (2. z)] BesselY[n + 0.5, z]
SphericalHankel[n_, z_] := SphericalBesselJ[n, z] + I SphericalBesselY[n, z]

j[n_] := SphericalBesselJ[n, ka]
y[n_] := SphericalBesselY[n, ka]
h[n_] := SphericalBesselJ[n, ka] + I SphericalBesselY[n, ka]

a[n_] = j[n] / h[n];
b[n_] = (ka * j[n - 1] - n * j[n]) / (ka * h[n - 1] - n * h[n]);

rcs = 0
Do[rcs += (I * ((-1)^n) * (n + 0.5) * (a[n] - b[n])), {n, 100}]

scatt = (landa / Sqrt[Pi]) rcs;

Length[rscs]

dataout = Transpose[{freq, Re[scatt], Im[scatt]}];

Export["C:\\Documents and Settings\\Nancy\\My Documents\\Data\\Theoretical\\4inspheretheor2to18pts1024.dat", dataout, "Table"];

rscs = .

```

REFERENCES

- [1] Dean L. Mensa, High Resolution Radar Cross-Section Imaging, Norwood, MA, Artech House, 1991.
- [2] Anil Kumar Kollipara, "A Physics Based Time-Frequency Analysis to Reduce Multi-Bounce and Clutter in Radar Imaging," Masters Thesis, University of Texas at Arlington, 2005.
- [3] E. F. Knott, J. F. Shaeffer and M. T. Tuley, Radar Cross Section, Second Edition, Norwood, MA, Artech House, 1993.
- [4] Nicholas C. Currie, Radar Reflectivity Measurement: Techniques & Applications, Norwood, MA, Artech House, 1989.
- [5] E. Oran Brigham, The Fast Fourier Transform and its Applications, Englewood Cliffs, NJ, Prentice-Hall, 1988.
- [6] W. G. Carrara, R. S. Goodman, and R. M Majewski, Spotlight Synthetic Aperture Radar: Signal Processing Algorithms, Norwood, MA, Artech House, 1995.
- [7] F. J. Harris, "On the use of windows for harmonic analysis with the discrete Fourier transform," Proceedings of the IEEE, vol. 66, no. 1, pp. 51-83, Jan 1978.
- [8] Stuart R. DeGraaf, SAR imaging via modern 2-D spectral estimation methods, IEEE Transactions on Image Processing, vol. 7, No. 5, 1998.
- [9] Greg McCarter, "Software or Hardware Gating-What's Best for RCS Measurements," Microwave Systems News, vol. 19, Issue 11, pp. 60-65, Nov. 1989.
- [10] B. D. Jersak, "Time Domain Analysis of Measured Frequency Domain Radar Cross Section Data," Masters Thesis, University of Texas at Arlington, 1988.
- [11] I. Daubechies, "Orthonormal bases of compactly supported wavelets," Comm. Pure and Applied Math., vol. 41, Nov. 1988, pp. 909-996.
- [12] Stephane Mallat, A Wavelet Tour of Signal Processing, Second Edition, Academic Press, 1998.

- [13] G. Strang and T. Nguyen, Wavelets and Filter Banks, Wellesley-Cambridge Press, Wellesley, MA, 1996.

BIOGRAPHICAL INFORMATION

Nancy Lanett graduated from the University of Texas at Arlington in 1997 with a Bachelor of Science in Electrical Engineering. She is currently pursuing a Master of Science in Electrical Engineering at the University of Texas at Arlington, expected graduation May, 2006. She has worked for Raytheon since 1997 where she is a member of the Advanced Products Center in McKinney, Texas. Current research interests include radar imaging, radar cross section measurements, antennas and signal processing.